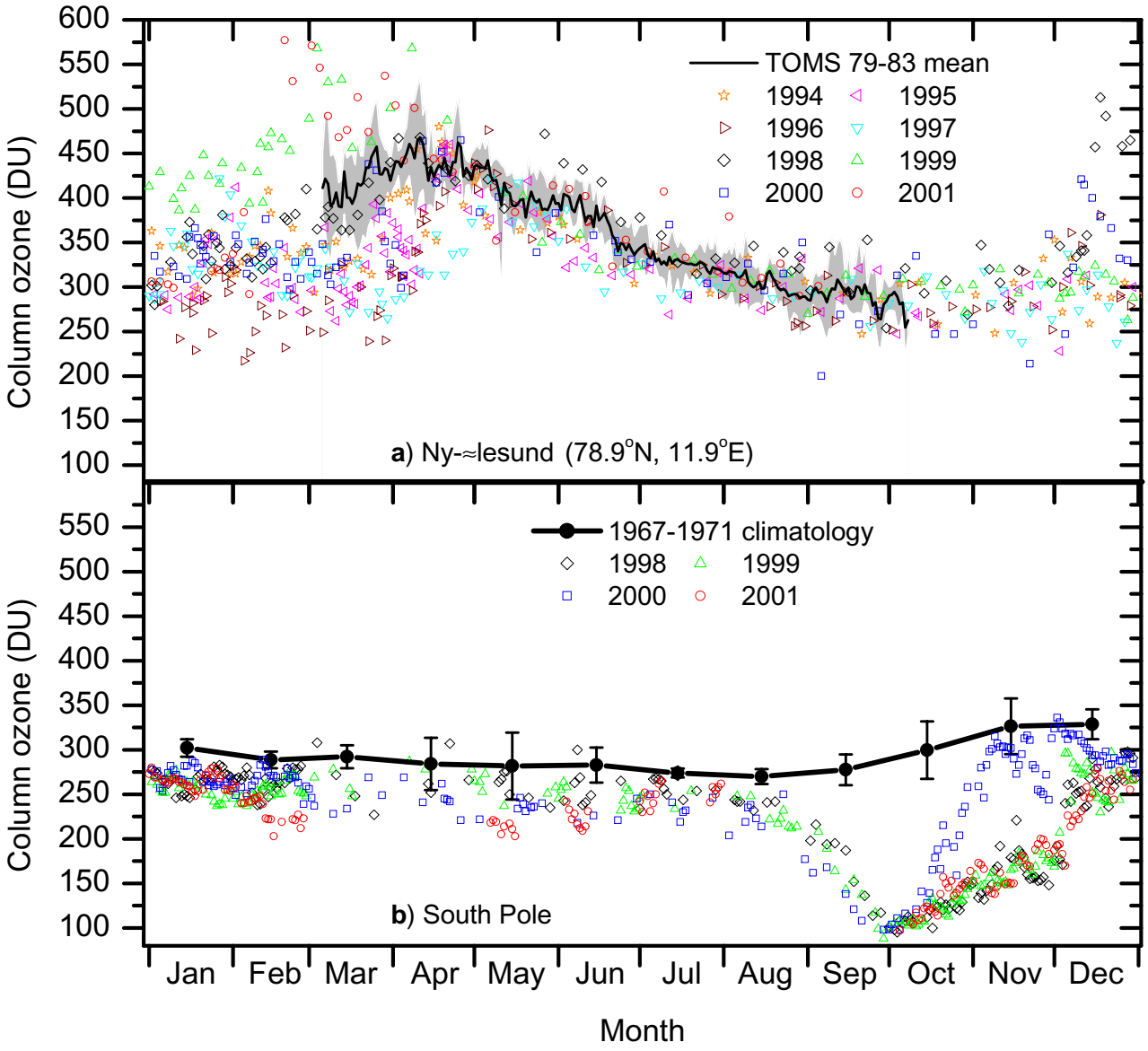

Figure 1.2-1. The column ozone determined from ozonesondes launched from Ny Alesund (a) and ozonesonde and Dobson measurements at South Pole (b) as a function of day of year. Symbols give individual measurements. The solid line is the daily TOMS mean column ozone for the Ny ≈lesund station from 1979 to 1983 with the shading indicating the range. A climatology for the South Pole from 1967-1971 is shown. (Courtesy Peter von der Gathen and Samuel Oltmans).

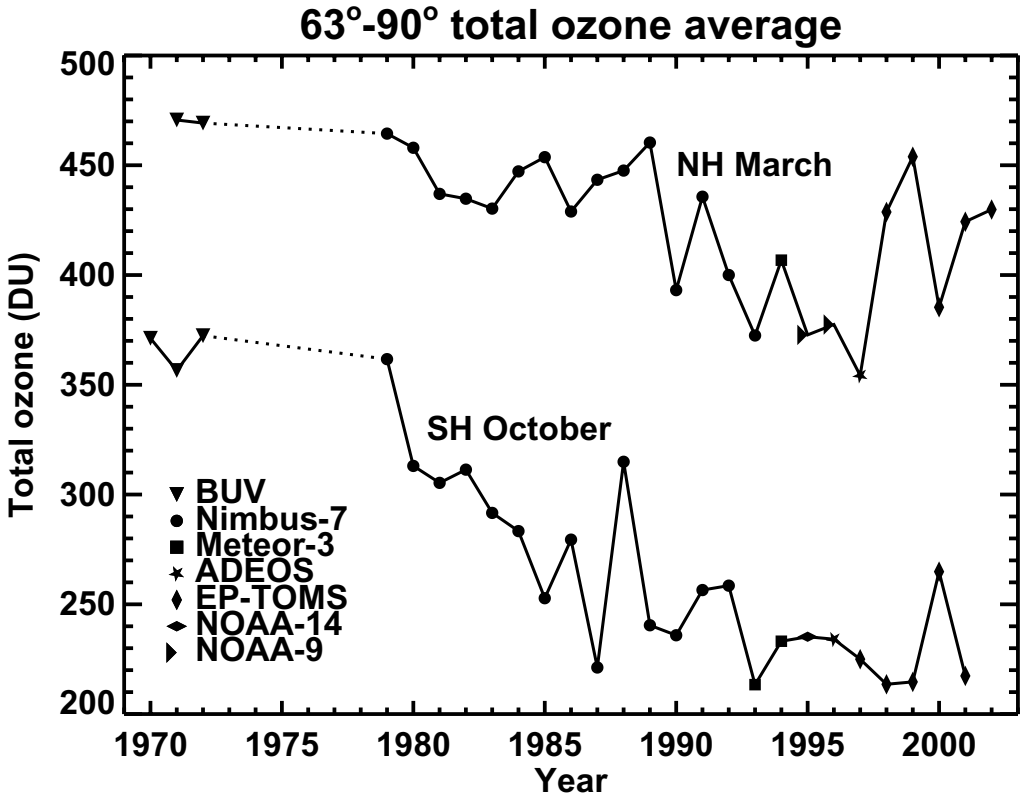

Figure 1.2-2. Total ozone poleward of 63˚ latitude in March in the Northern Hemisphere and October in the Southern Hemisphere. Symbols indicate the satellite data that have been used in the different years. This is an update from Newman *et al.* (1997).

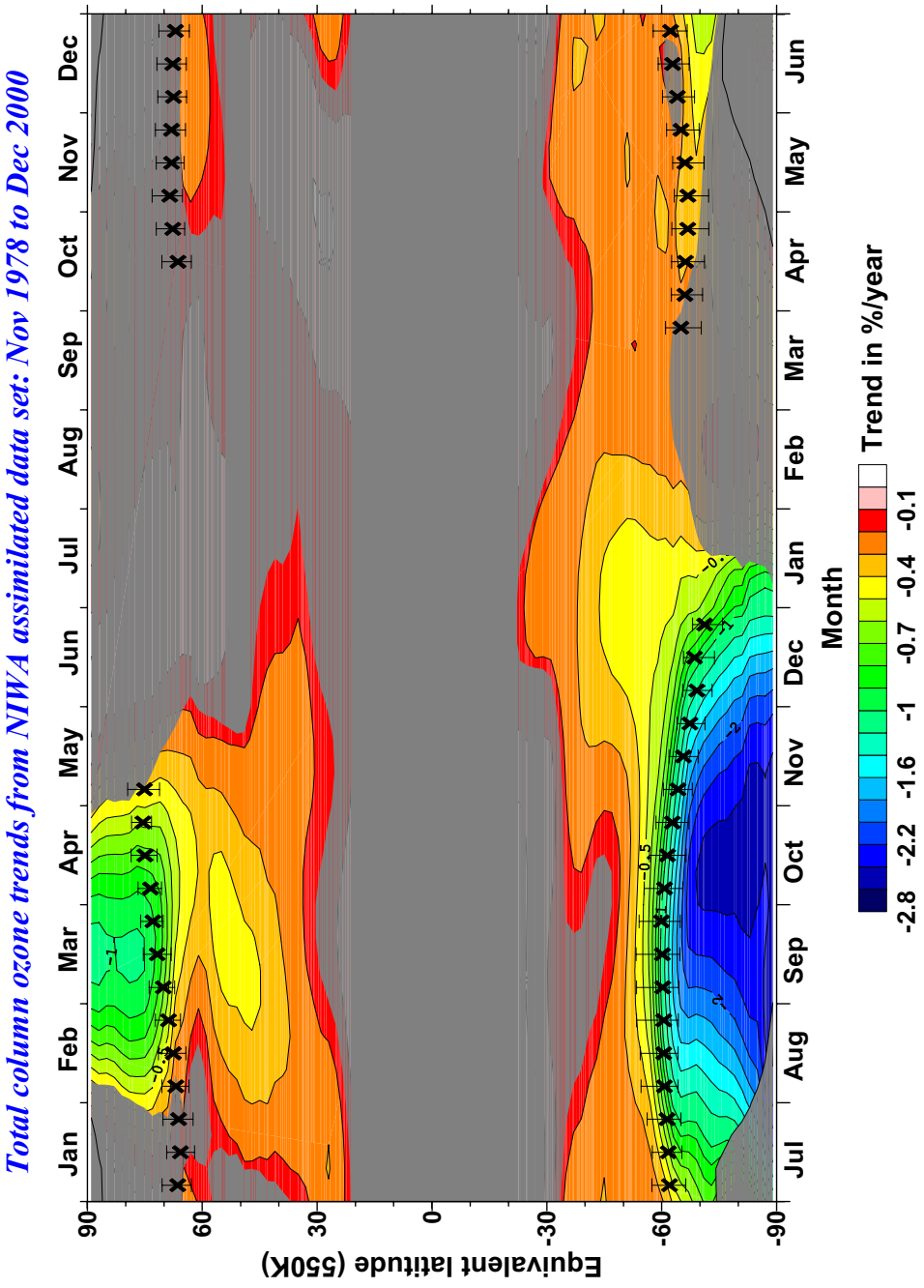

Figure 1.2-3. Total column ozone trends as a function of equivalent latitude and season using corrected TOMS and GOME from November 1978 to December 2000. Shaded regions indicate where trends are statistically insignificant (at 95% confidence). The crosses show the mean position of the vortex (remnant) edge(s) over the time period when the position could be determined, and the 'error bars' on each cross show the mean width of the vortex boundary (Nash *et al.,* 1996). The equivalent latitude is calculated on 550-K isentropic surface (Bodeker *et al.,* 2001).

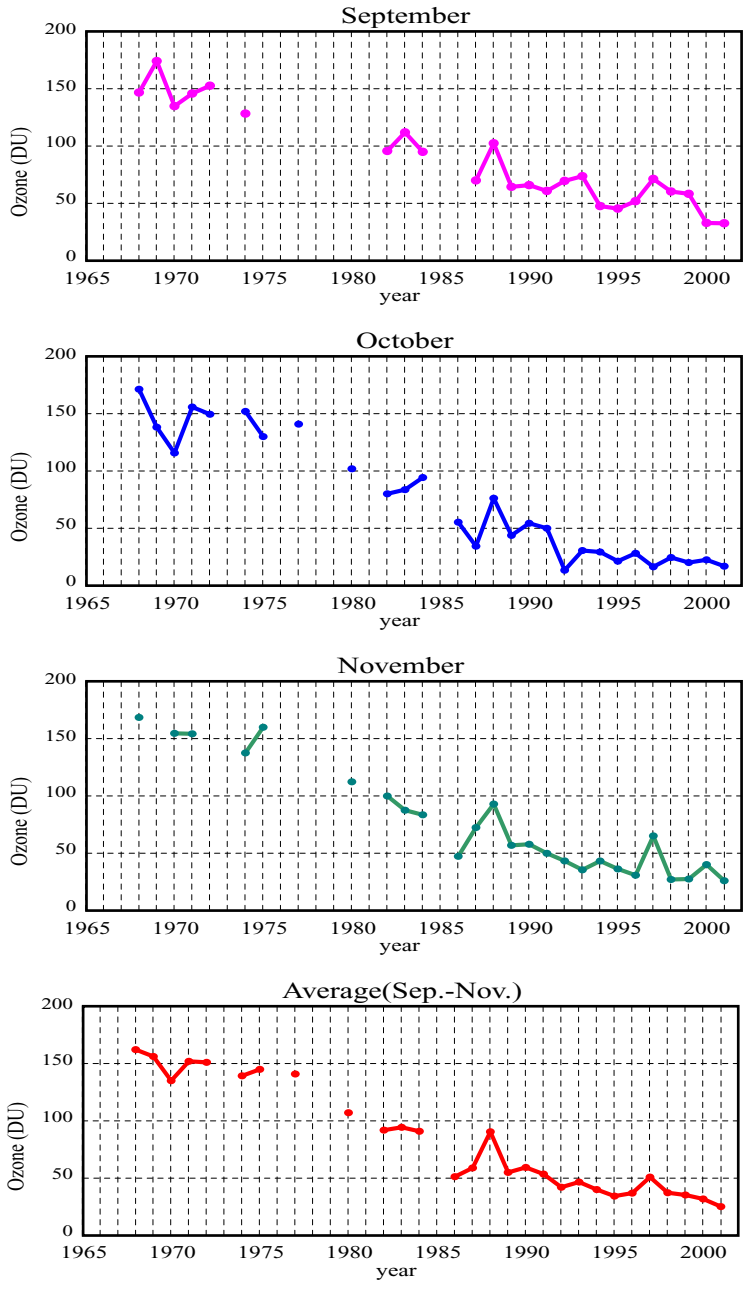

Figure 1.2-4. Partial column ozone in the 12- to 20-km layer in September-October-November over Syowa in Antarctica from 1968 to 2001. Update of Figure 4-27 of WMO (1999) by Japan Meteorological Agency.

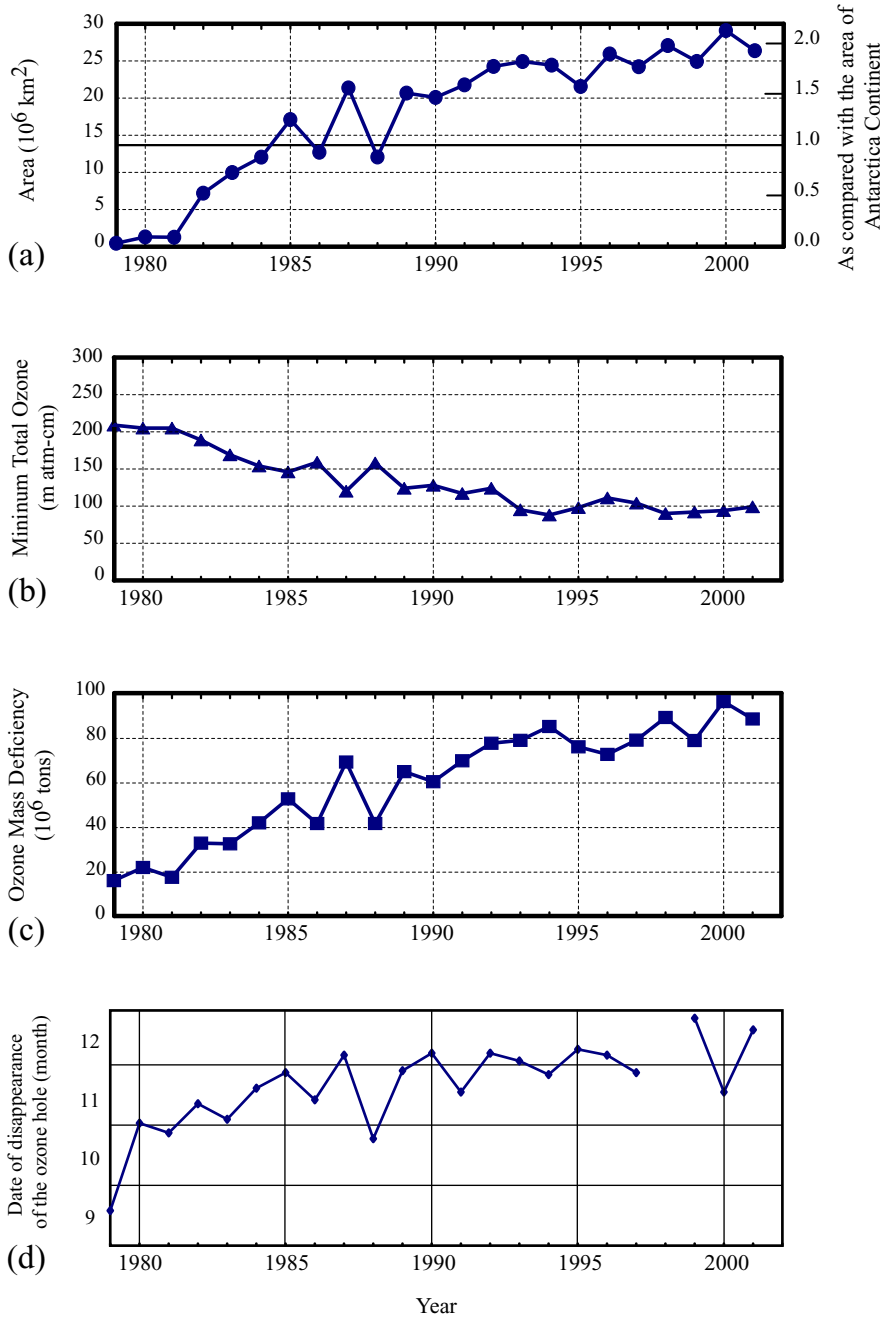

Figure 1.2-5. Evolution of the Antarctic ozone hole (defined by total ozone values below 220 DU) based on satellite data for the period 1 September-15 December of each year. Maximum area covered by ozone hole values (in millions km2) (a), minimum total column ozone measured each year (b), ozone mass deficiency from 300 DU integrated for 105 days (in Mt) (c) and date of disappearance of the ozone hole values (d) (Uchino *et al.,* 1999, data updated to 2001).

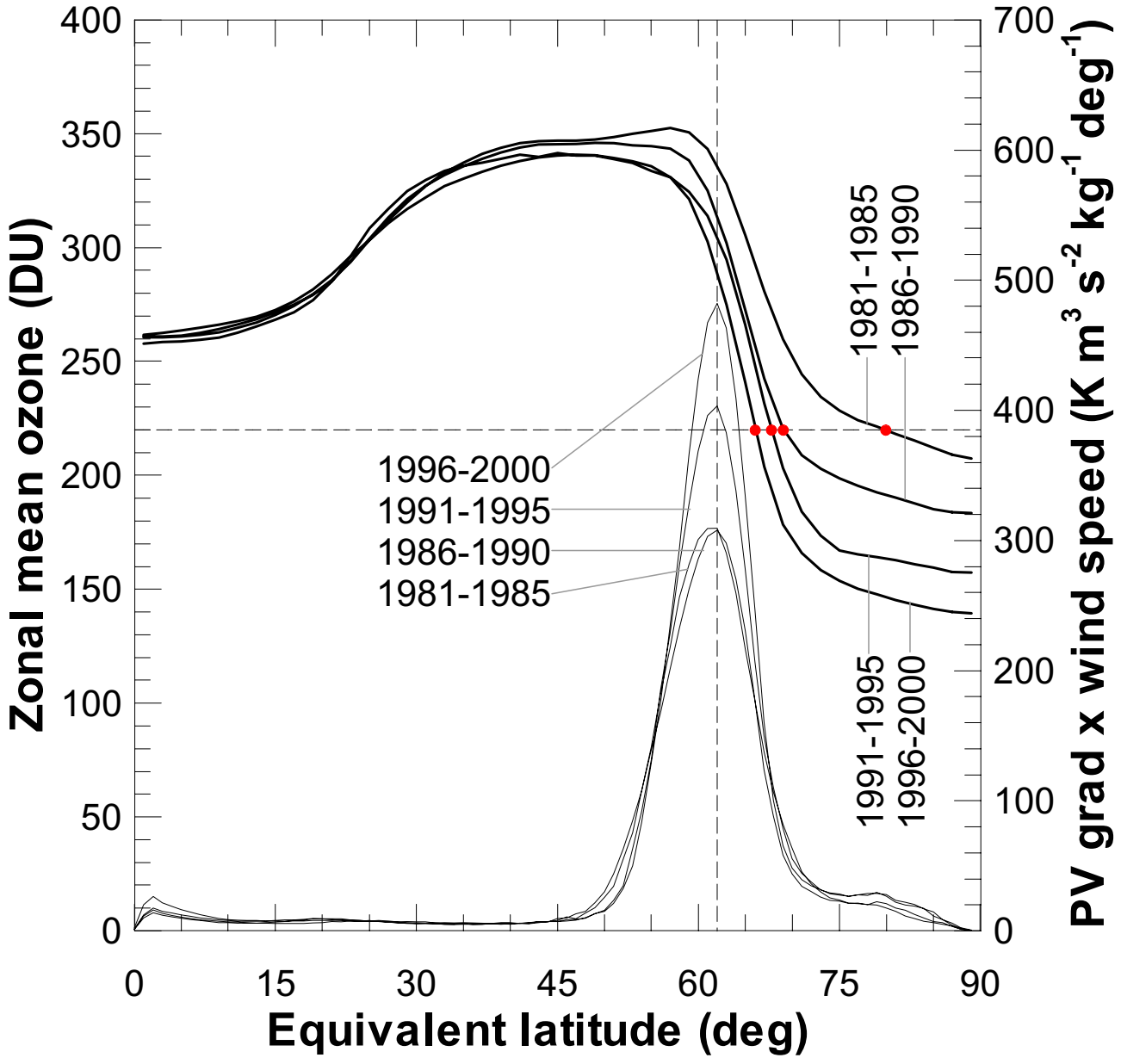

Figure 1.2-6. October average zonal mean total column ozone (thick solid lines plotted against the left ordinate) and October average vortex strength (gradient of potential vorticity multiplied by zonal wind speed; thin solid lines plotted against the right ordinate) for each of the four analysis periods (Bodeker *et al.,* 2002).

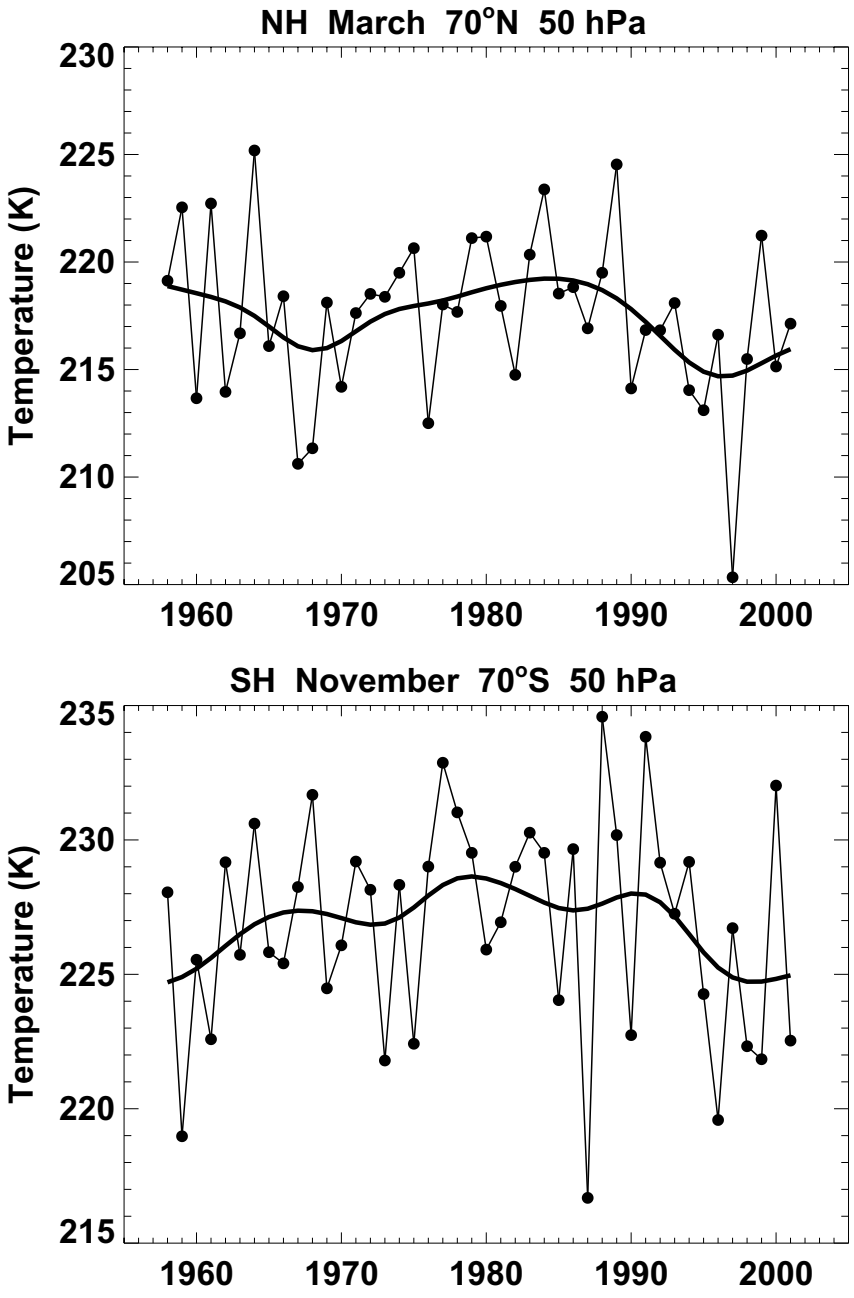

Figure 1.2-7. Time series of zonally averaged 50hPa temperature at 70˚N in March (top panel) and 70˚S in November (bottom panel). The data are derived from the NCEP/NCAR reanalysis data. The thick solid line is the smoothed time series (following Randel and Wu, 1999a).

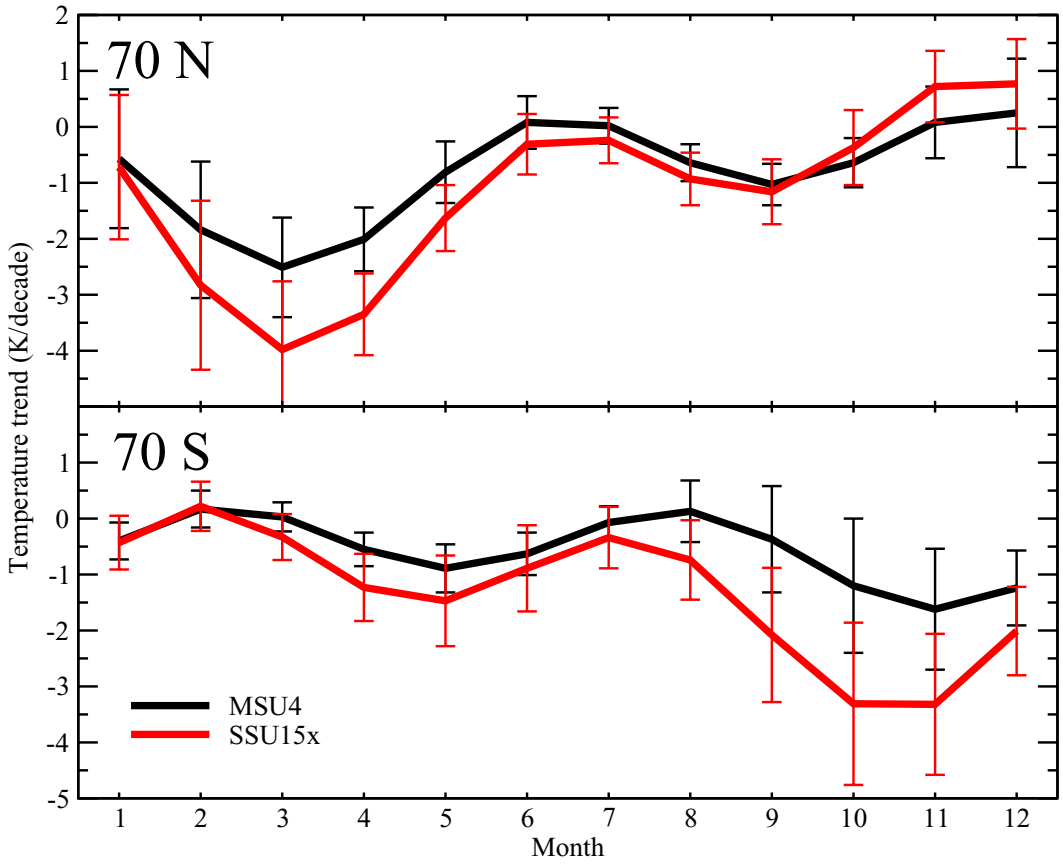

Figure 1.2-8. Temperature trends for the period 1979-1998 at 70˚N (top panel) and 70˚S (bottom) for MSU-4 (black line) and SSU-15X (red line) for each month of the year.

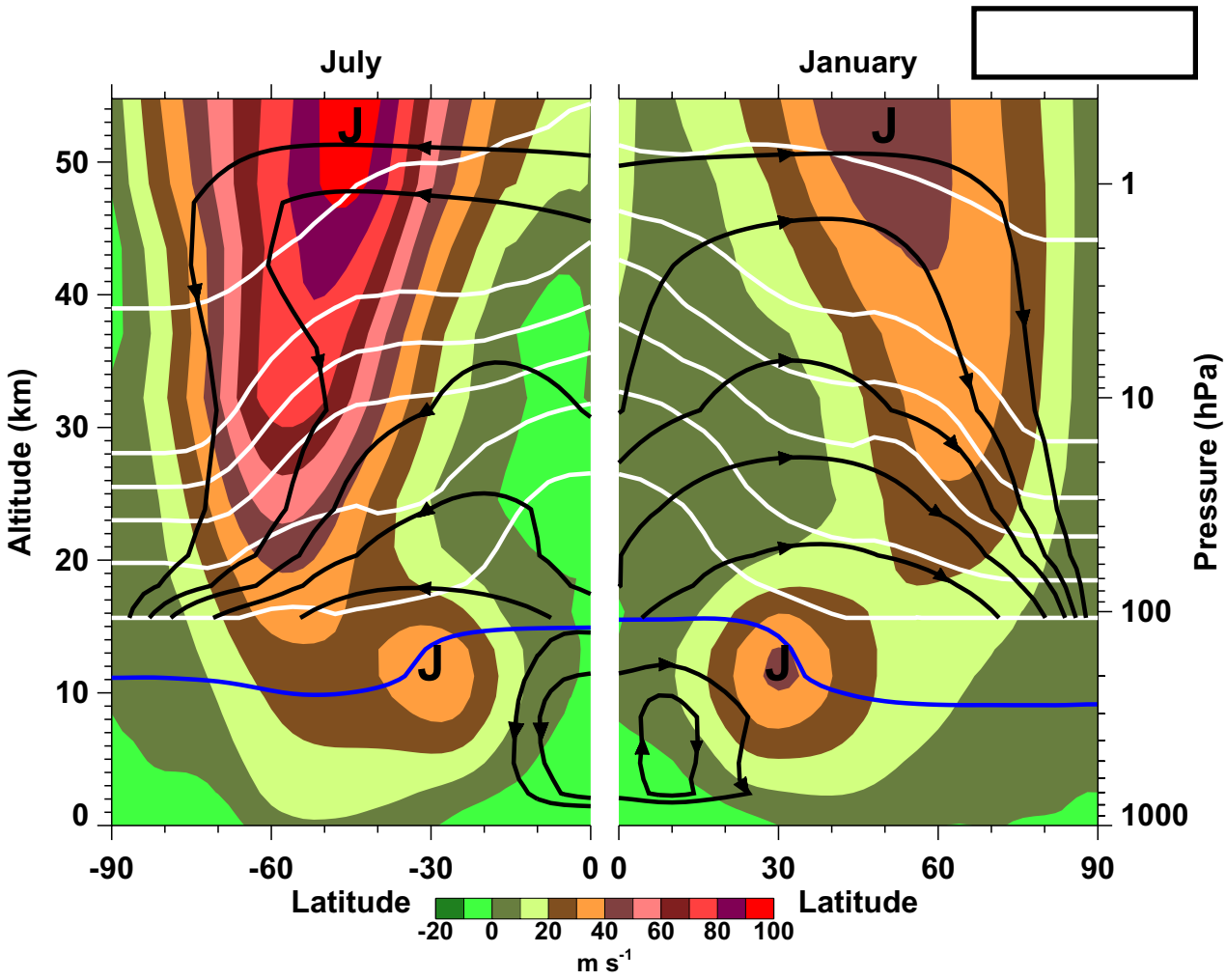

Figure 2.1-1. Zonal-mean sections of zonal velocity (shaded), the mean meridional stream function (black lines) and an atmospheric trace gas (white contours) for midwinter (July in the Southern Hemisphere and January in the Northern Hemisphere). The data are obtained from multi-annual climatologies. The figure illustrates the stronger polar night jet in the Southern Hemisphere, the stronger subtropical jet in the northern winter, along with consistent differences in the strength and structure of the mean meridional circulation and trace gas distributions.

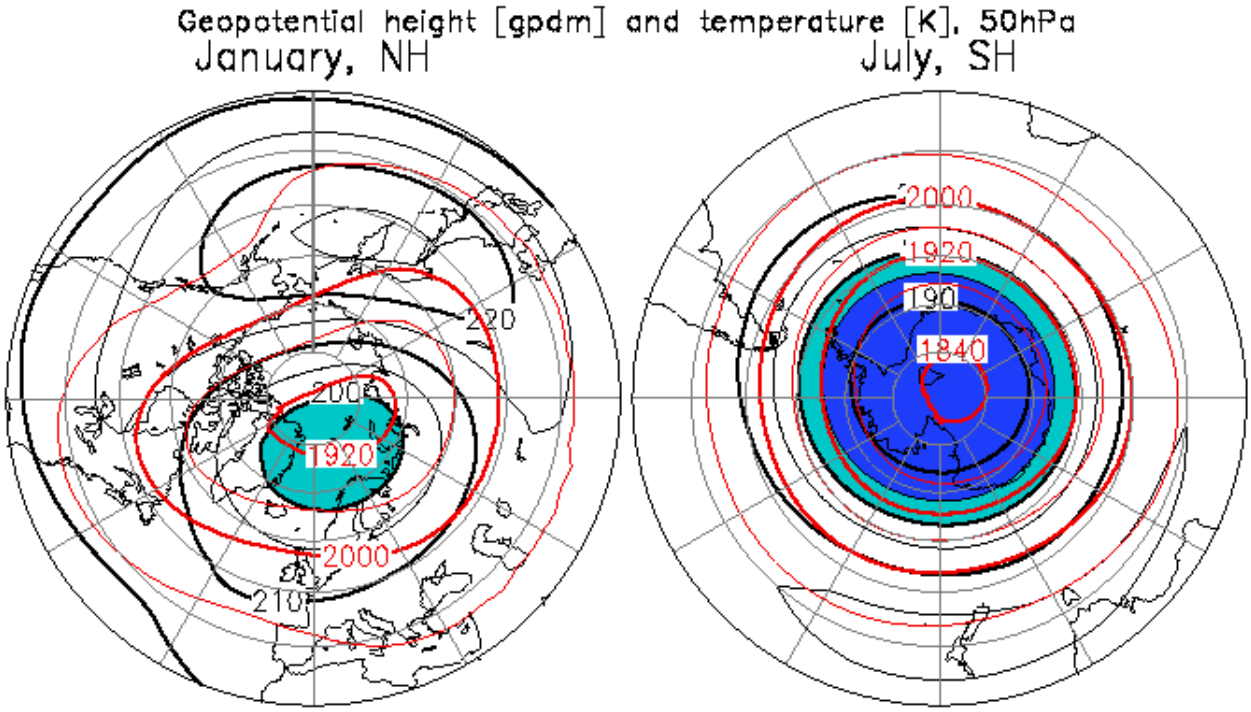

Figure 2.1-2. Polar stereographic projections for January in the Northern Hemisphere and July in the Southern Hemisphere. The geopotential height (red contours) and temperature (black contours) for 50 hPa are shown. Light blue shading indicates regions colder than 200 K, while dark blue shading shows regions colder than 195 K. Data are 19-year means from the UKMO-processed TOVS data (Scaife *et al.* 2000b).

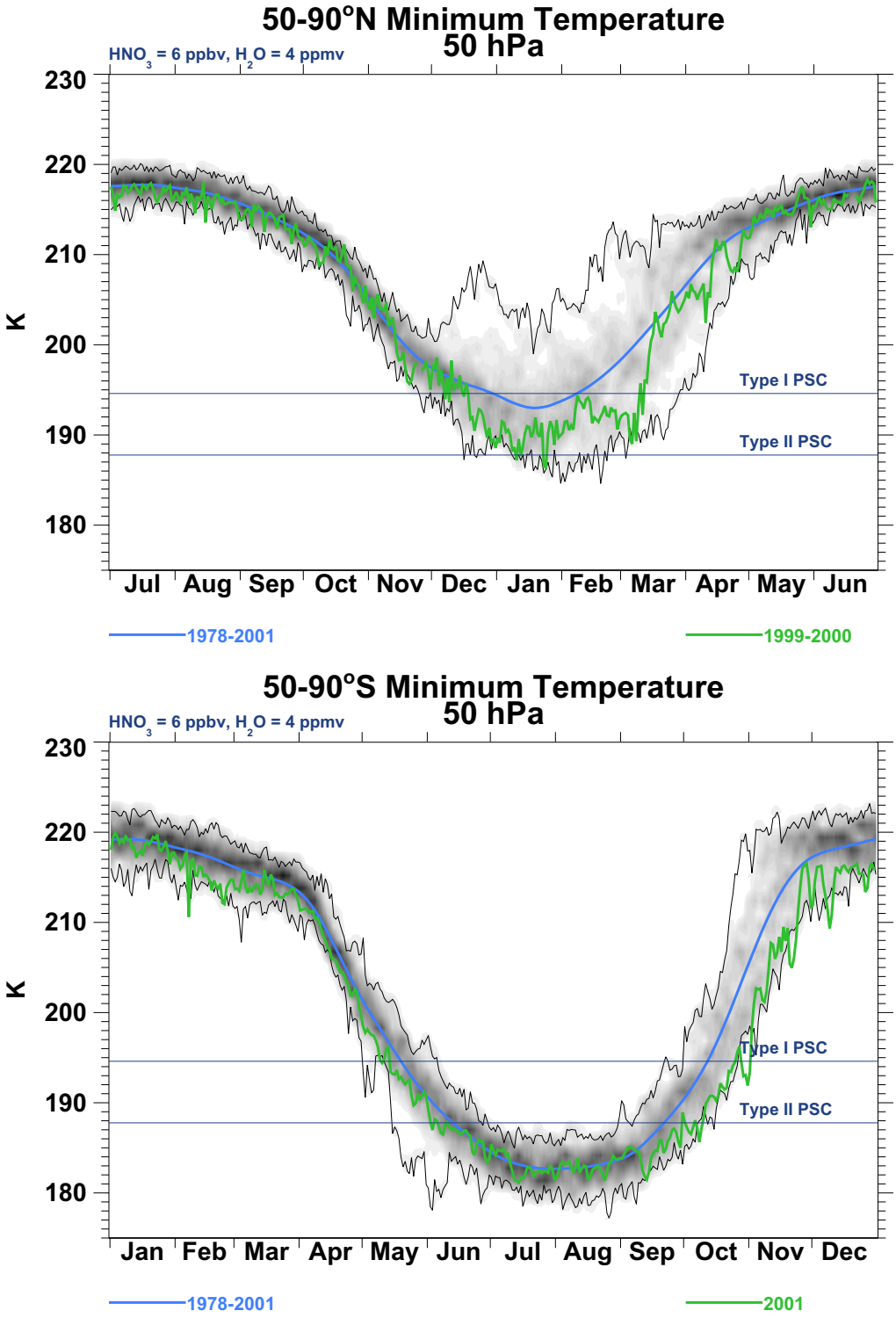

Figure 2.1-3. Time series showing binned distributions of polar minimum temperatures for the Arctic (top panel) and Antarctic (bottom panel). The data are derived from daily minimum temperatures at 50 hPa observed poleward of 50˚. The blue line indicates the average minimum temperature, while the thin black lines show the extrema of the distribution. The Antarctic is offset by six months to contrast the seasonal cycles. Data are from the NCEP/CPC analyses.

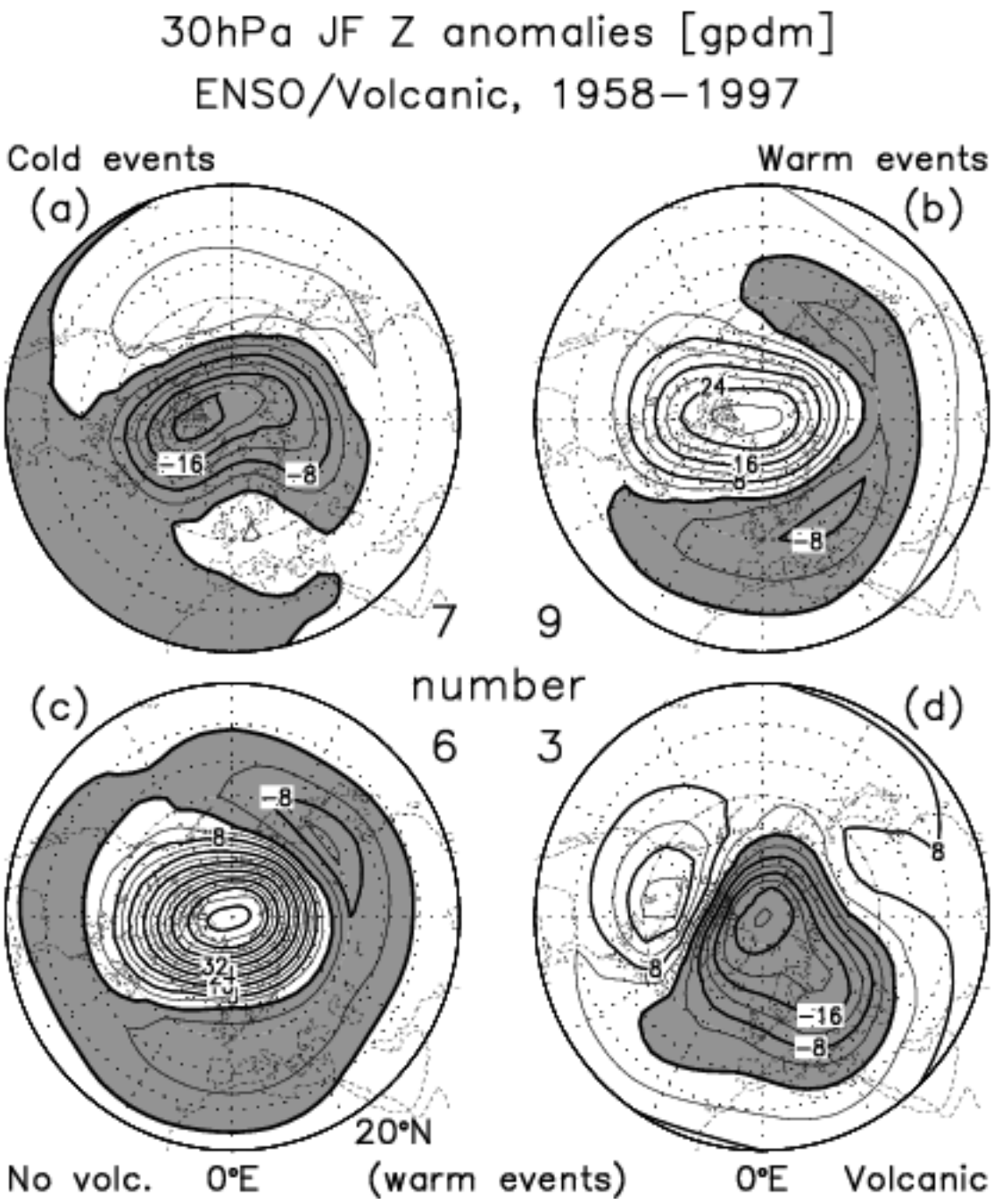

Figure 2.1-4. The anomalies in January/February 50-hPa geopotential height revealed by composite anomaly plots for ENSO and volcanic events, as determined from FUB analyses. The two top panels are (a) the composite anomaly of the seven winters with ENSO cold events and (b) that for the nine warm events. The anomalies are in gpdm and are relative to the mean of the years with no ENSO events. The lower two panels show the warm-event anomalies of panel (b), but further split into the six years with no volcanic events (panel c) and the three years with them (panel d). These results are updated from van Loon and Labitzke (1987) and Labitzke and van Loon (1989).

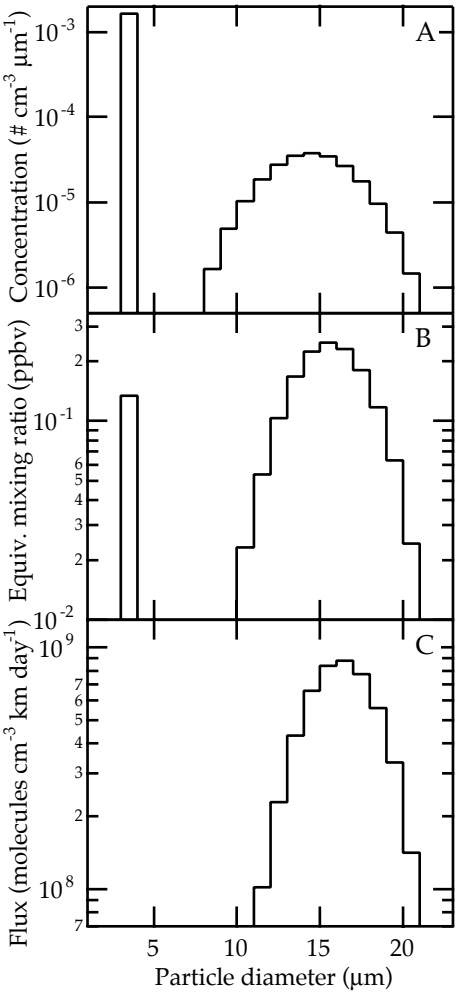

Figure 2.2-1. Results from the statistical simulation of NO_y values observed by the ER-2 NO_y instrument on 20 January 2000 (Fahey *et al.,* 2001). Panels show the adjusted best-fit size distribution and number concentration (A), the equivalent gas-phase mixing ratio of HNO_3 derived from the distribution (B), and the derived flux of HNO_3 at 60 hPa (~19.5 km) (C). The size distribution is given by the Gaussian functions in the caption of Figure 3 adjusted to account for size-dependent sampling efficiency. The adjustments, which are in addition to a basic particle enhancement factor of 12.8, range from +30% to –10% over the size range and are calculated with a fluid dynamical model of the particle separator. The concentration integral of the large (small) mode is 2.3 x 10^{-4} cm^{-3} (2 x 10^{-3} cm^{-3}) with an estimated uncertainty of ±30%. The lower limit of the vertical axis in (A) corresponds to the detection of a single particle over the 800-s observation period. The total gas-phase HNO_3 of the large (small) mode is 1.5 ppbv (0.2 ppbv). The HNO_3 flux of the combined distribution is 5 x 10^9 molecules cm^{-3} km day^{-1} or 2.2 ppbv km day^{-1} at 60 hPa.

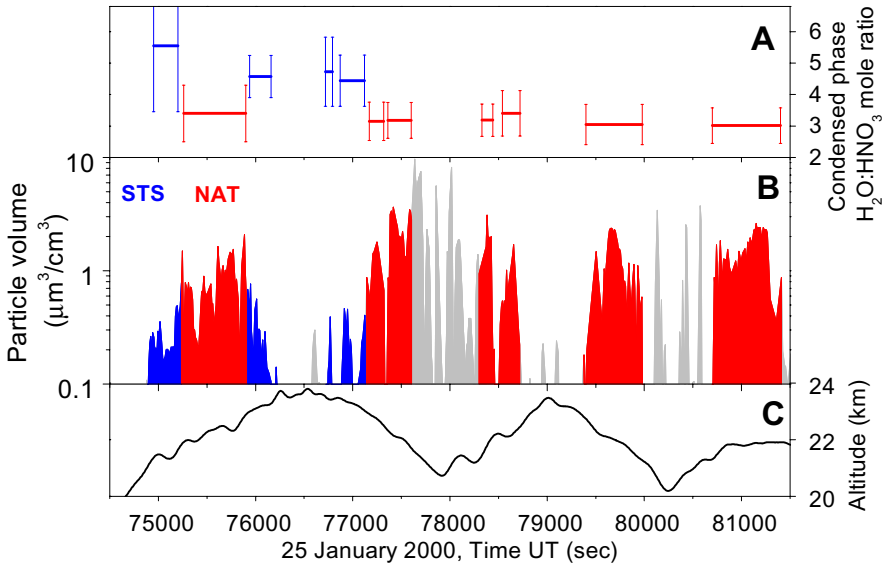

Figure 2.2-2. *In situ* observations of PSCs using an aerosol mass spectrometer, showing particles with a HNO_3/H_2O ratio consistent with supercooled $HNO_3/H_2SO_4/H_2O$ droplets (Voigt *et al.*, 2000b).

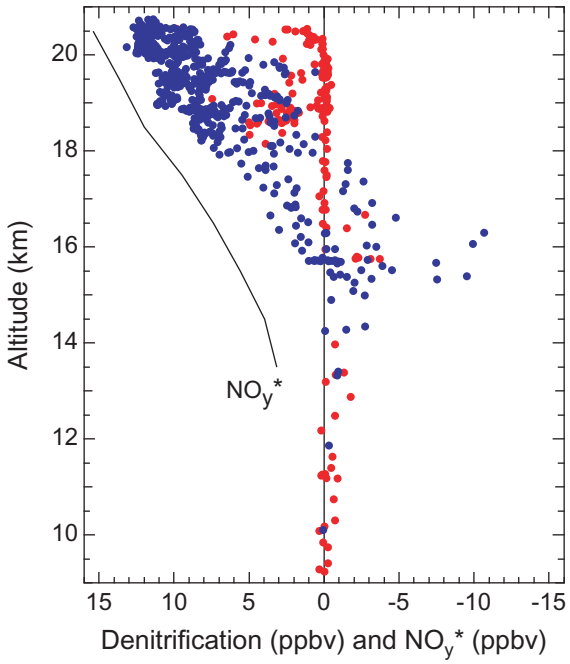

Figure 2.2-3. Vertical profiles of redistributed NO_y in the 1999-2000 Arctic vortex. Positive values of denitrification represent NO_y removal. Blue and red symbols represent measurements made at greater than 70˚N and less 70˚N equivalent latitude, respectively. The solid black line representing NO_y^* was determined from altitude bin-averaged N_2O values for measurements made throughout the winter at equivalent latitudes greater than 70˚N. This term represents the maximum available NO_y at a given altitude. Maximum ER-2 flight altitudes of 20 to 12 km represent a potential temperature of approximately 460 to 475 K. Adapted from Popp et al. (2001).

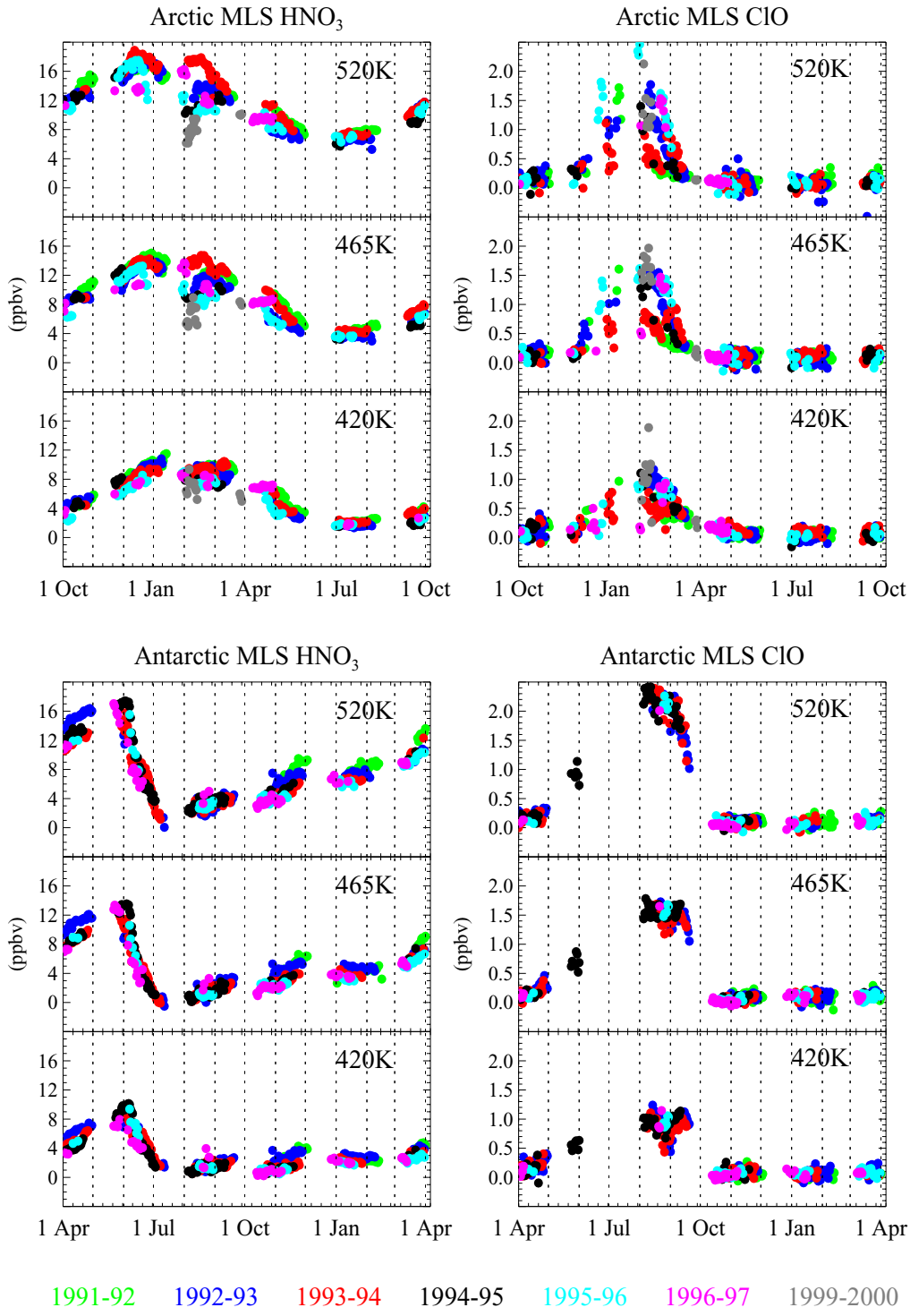

Figure 2.2-4. Time series of UARS MLS HNO_3 (left, ppbv) and ClO (right, ppbv) at 520†K (~21km), 465 K (~19km), and 420 K (~17km) for both the Northern (top) and Southern (bottom) Hemispheres. Values shown are averages of data points with solar zenith angle < 88 degrees (daylight) in the 70- to 80-degree equivalent latitude bin. These values represent the best estimates of the abundances at these particular potential temperature surfaces based on the MLS measurements; it should be borne in mind, however, that correlations between these levels may have been introduced either during the retrieval process (since the retrieval pressure grid is finer than the width of the averaging kernels) or through interpolation of the retrieved data onto potential temperature surfaces, and thus the true number of completely independent pieces of information is likely to be less than the number of surfaces shown here. For the daily averages in this equivalent latitude bin the precision is roughly 0.15 ppbv for HNO_3 and 0.05 ppbv for ClO. Different years are represented by different colors as indicated in the legend. The x-axis tick mark increment is 10 days; dotted vertical lines demark calendar months. The 1991-1997 and 2000 data are adapted from Santee *et al.* (1999) and (2000), respectively.

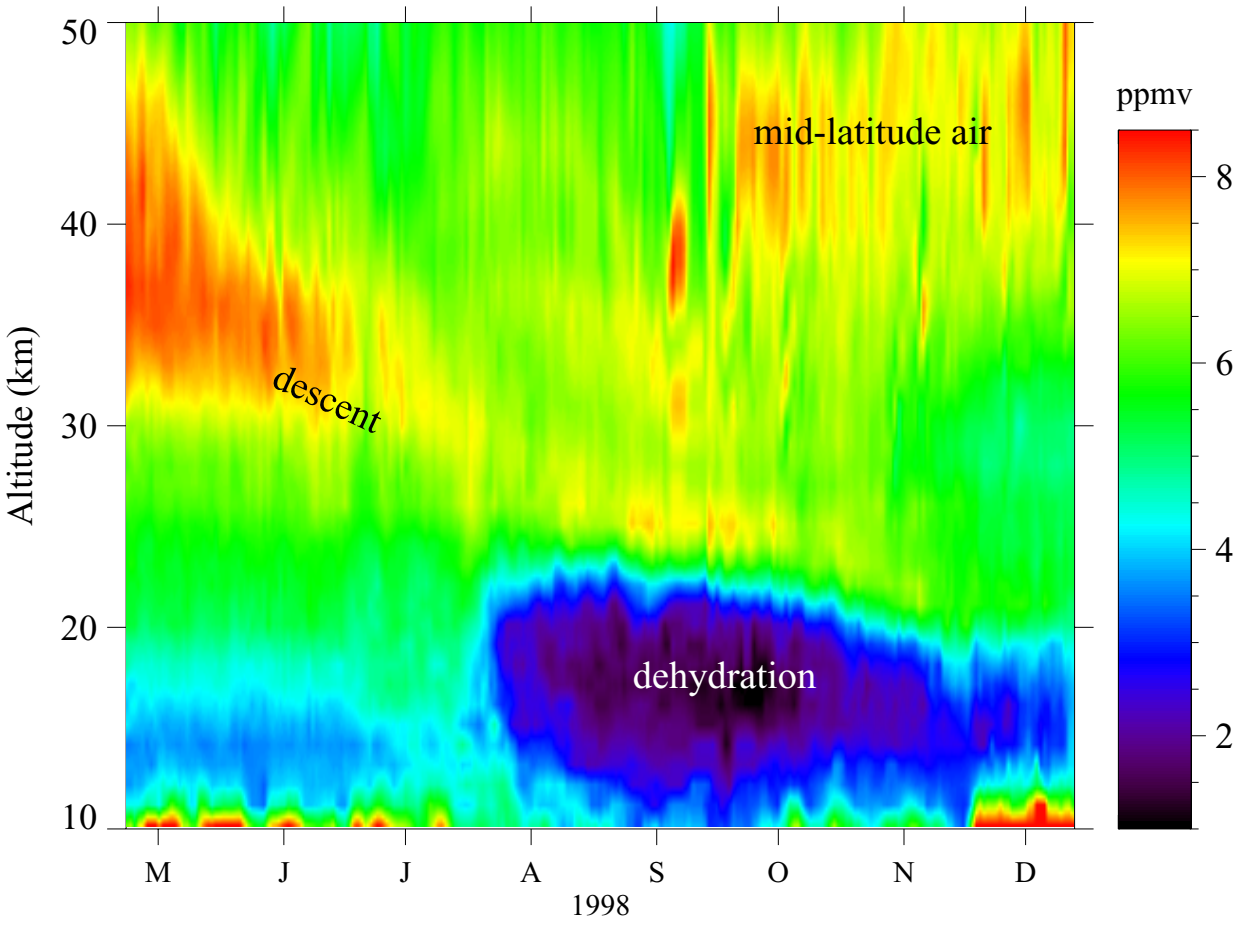

Figure 2.2-5. The water vapor mixing ratio as measured by POAM in the Southern Hemisphere from April 27, 1998 to December 12, 1998. Profiles are obtained from daily averages of the POAM measurements, which generally provides 14 measurements/day. Measurements from both inside and outside of the vortex are included. Adapted from Nedoluha *et al.* (2000).

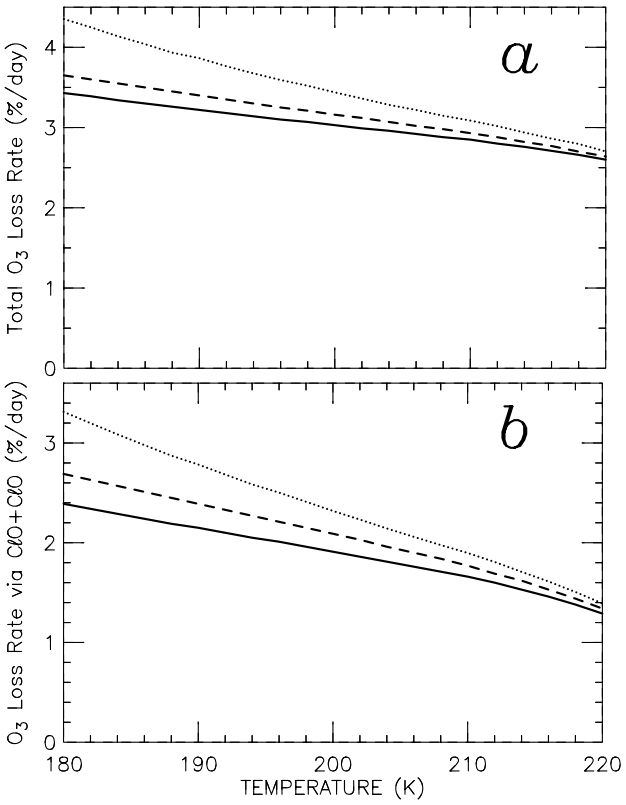

Figure 2.3-1. Panel *a*. Calculations of 24 hour average total chemical ozone loss rate for an air mass at 70∞S, 50 mbar, as a function temperature for mid-September conditions (e.g., ClO+2*ClOOCl=2 ppb, BrO+BrCl=10 ppt, O_3= 2 ppm, declination=5∞S) assuming *Case 1*: JPL 00-3 kinetics (solid line); *Case 2*: The Bloss *et al.* (2001) value for k_{1a} and the noontime concentration of ClO fixed at the same value used in Case 1 (dotted line); *Case 3*: The Bloss *et al.* value for k_{1a} and the noontime concentration of ClO+2*ClOOCl fixed at the same value used in Case 1 (dashed line). Panel *b*. Same as *a*, except chemical loss rates due to the ClO+ClO cycle are shown. *Case 2* approximates the effect of the Bloss *et al.* value for k_{1a} on a model calculation constrained by measured ClO. *Case 3* approximates the effect of Bloss *et al.* k_{1a} within a free running CTM or GCM, where ClO and ClOOCl are allowed to equilibrate. From Bloss *et al.* (2001).

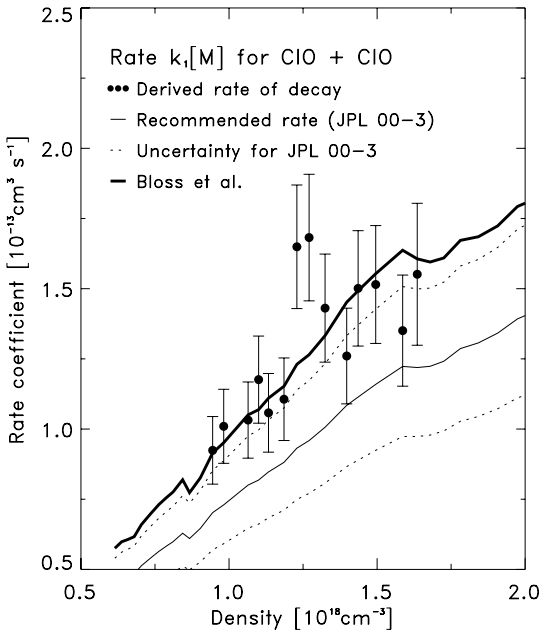

Figure 2.3-2. Derived rate of decay of ClO (points with 1σ error bars) from atmospheric observations of ClO obtained in the Arctic vortex during SOLVE-THESEO 2000 compared to the product of $M*k_{1a}$ from the JPL 00-3 recommendation (thin solid line) and from the laboratory study of Bloss *et al.* (2001) (thick solid line). Uncertainties for the JPL 00-3 rate are given by the dashed lines. Uncertainties for the laboratory measurement of Bloss *et al.* are not shown for clarity, but they are approximately the same size as the error bars for the results based on the ClO observations. From Vˆmel *et al.* (2001).

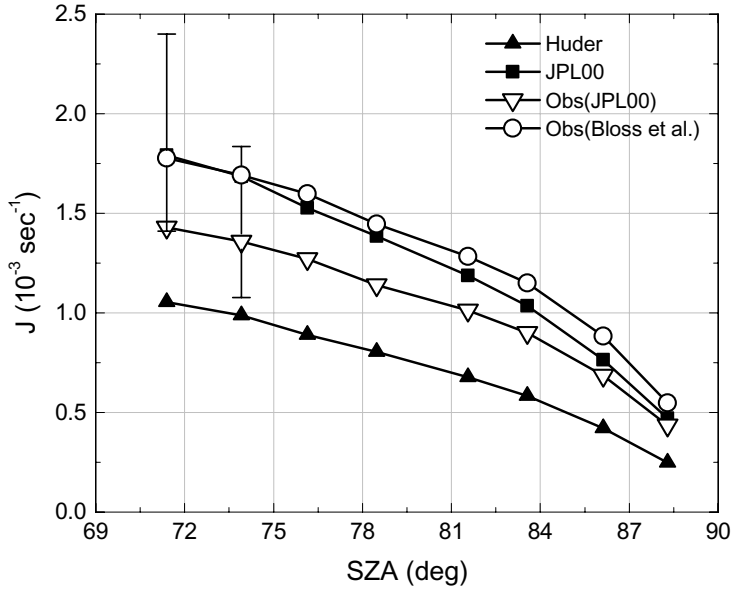

Figure 2.3-3. Value for the photolysis rate of ClOOCl, J_{1b}, as a function of solar zenith angle (SZA), derived from atmospheric measurements of ClO and ClOOCl assuming the JPL 00-3 value for k_{1a} (open triangle) and assuming the Bloss *et al.* (2001) value for k_{1a} (open circle). Error bars represent a propagation of 1σ uncertainties in the measurements of ClO and ClOOCl onto the computed photolysis rate. Values of J_{1b} found using a radiative model for ClOOCl absorption cross sections from JPL 00-3 (solid square) and from Huder and DeMore (1995) (solid triangle) are also shown. From Stimpfle *et al.* (2002). **NOTE: The original version of this paper has been withdrawn; we anticipate it will be re-submitted prior to the Les Diablerets meeting. If not, this figure will be removed.**

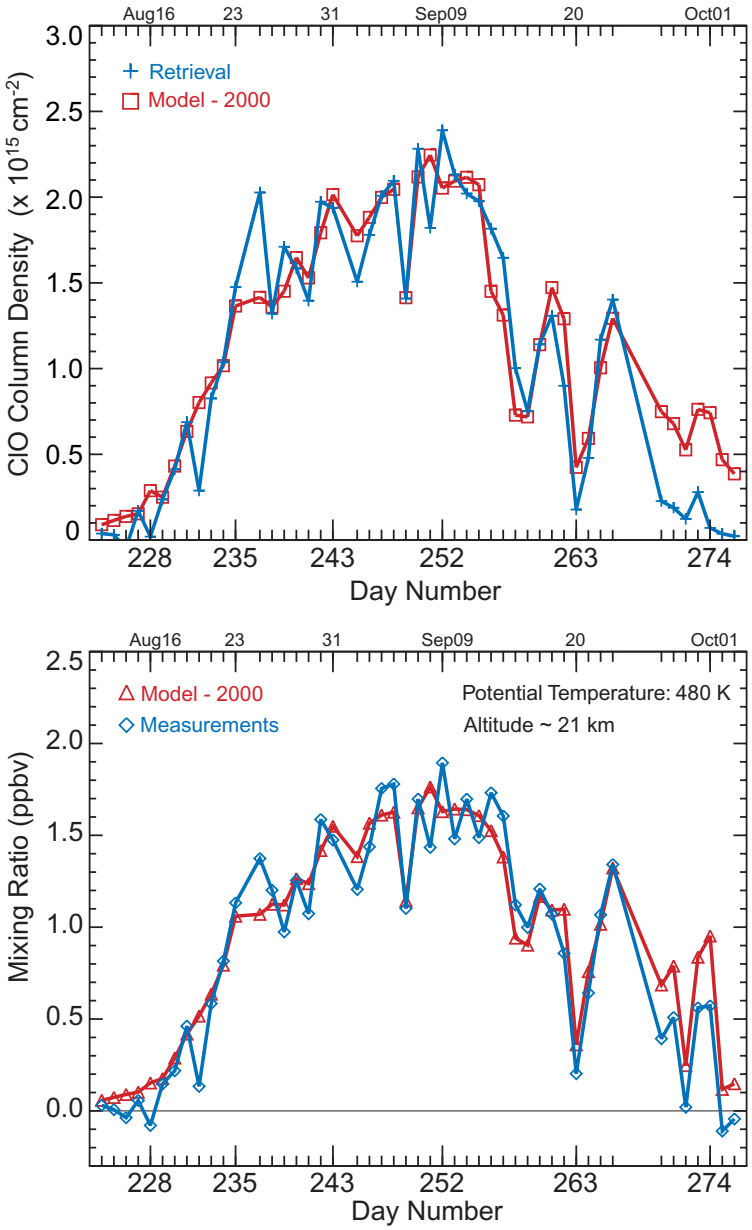

Figure 2.3-4. *Top Panel.* Retrieved ClO column density (day-night difference) for August 11, 2000 through October 4, 2000 over Scott Base, Antarctic (78˚S) (solid line) and the same quantity calculated using the SLIMCAT model assuming JPL 97-4 kinetics (dashed line). *Bottom Panel.* Same as top panel, except for ClO mixing ratio (day-night difference) at 480 K. From Solomon *et al.* (2002).

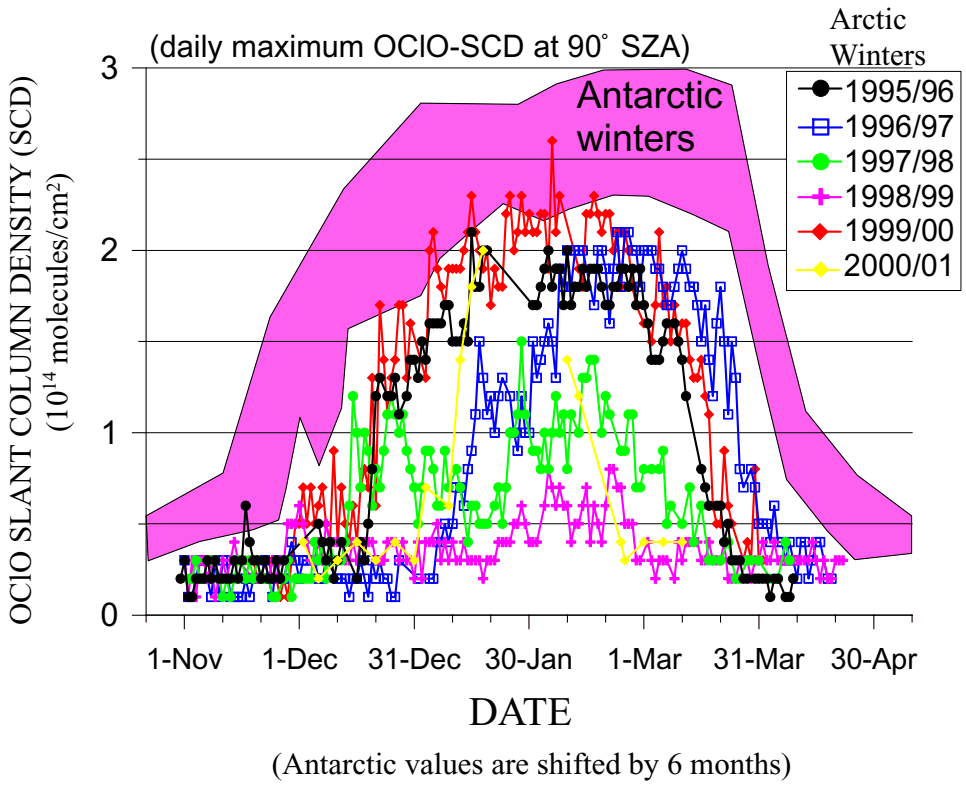

Figure 2.3-5. Slant column density (SCD) of OCO measured by GOME for a number of Arctic and Antarctic winters. The time associated with the Antarctic measurements has been shifted by six months, to facilitate comparison with the Arctic observations at comparable seasons. From Wagner *et al.* (2001, 2002).

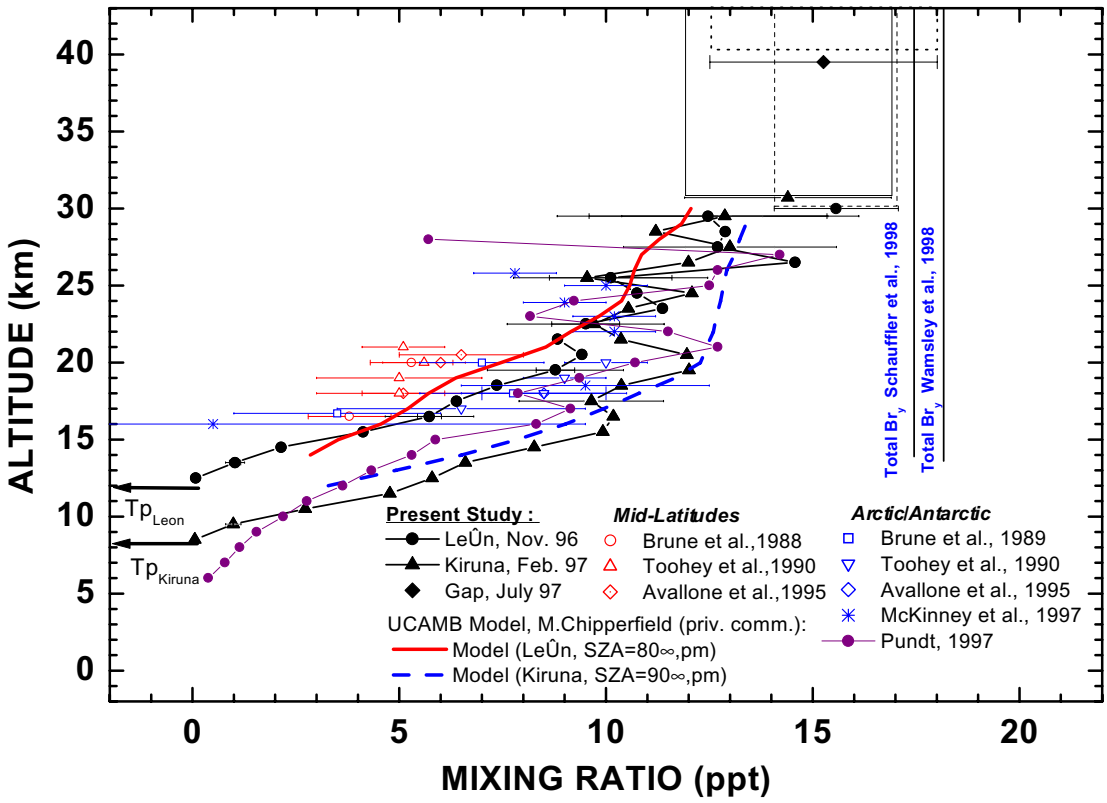

Figure 2.3-6. Measurements of profiles of BrO obtained at mid-latitudes, the Arctic, and the Antarctic by the in situ resonance fluorescence technique (red and blue open symbols and blue *) and by the remote differential optical absorption spectroscopy (DOAS) technique (closed symbols). Also shown are two estimates of total inorganic bromine loading at the top of the atmosphere based on measured abundances of brominated source gases (thin vertical lines). Calculations of profiles for BrO from the SLIMCAT model, appropriate for conditions of the DOAS observations of BrO from León, Spain (42.6˚N) and Kiruna, Sweden (67.9˚N), are shown by the red solid and blue dashed lines. Harder *et al.* (1998) should be consulted for the full citation of the references given on the figure. From Harder *et al.* (1998).

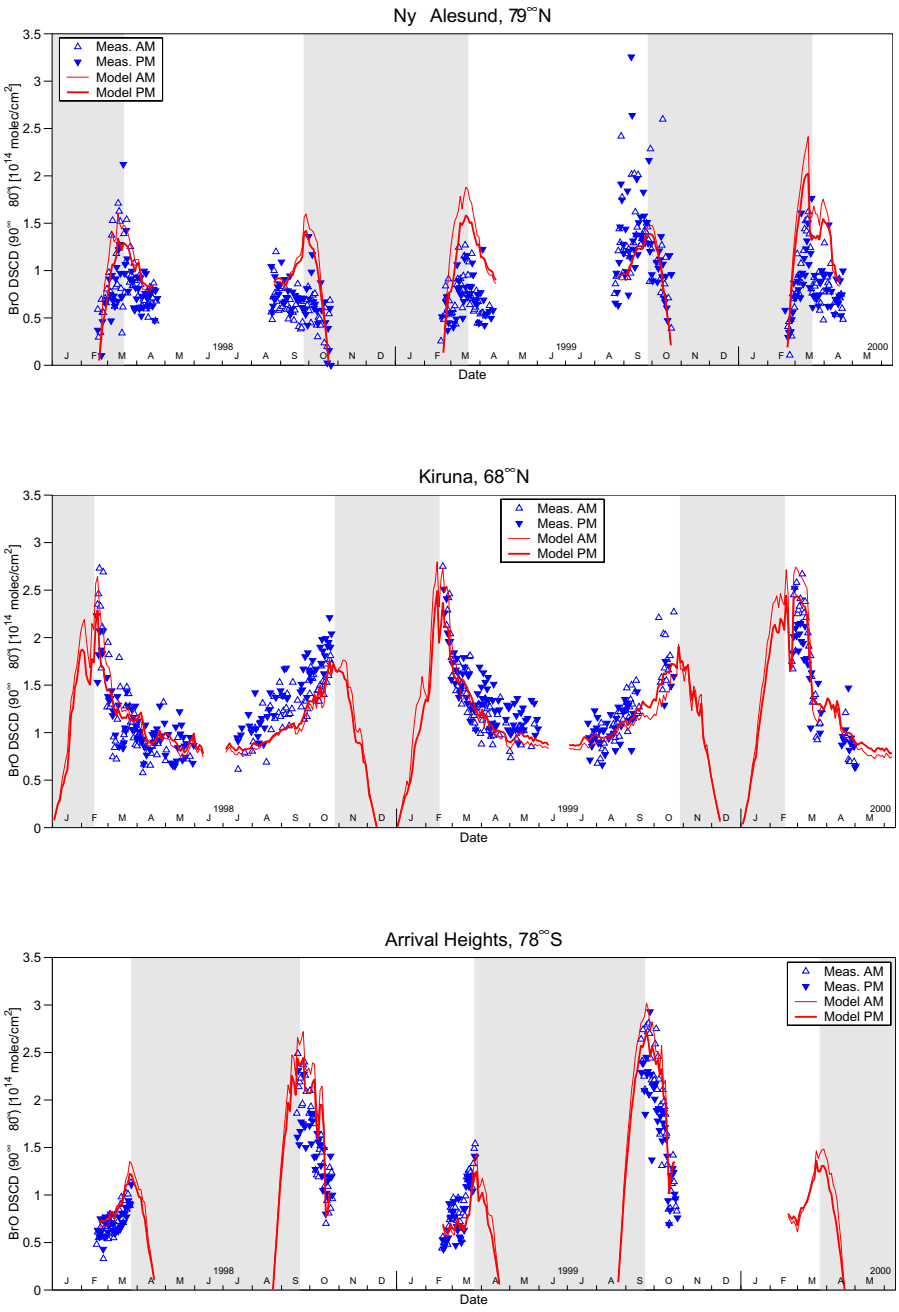

Figure 2.3-7. Comparison of measured and modeled differential slant column densities of BrO over Ny Ålesund, Spitsbergen (78.9˚N), Kiruna, Sweden (67.9°N), and Arrival Heights, Antarctica (78˚S). The differential slant columns are found from observations and model results obtained between solar zenith angles of 90˚ and 80˚ for the morning (AM) and evening (PM). However, when a solar zenith angle of 80˚ is not reached at high latitude (shaded regions), local noon values are used as a reference instead. Calculated values of BrO are from the SLIMCAT model. From Sinnhuber *et al.* (2002).

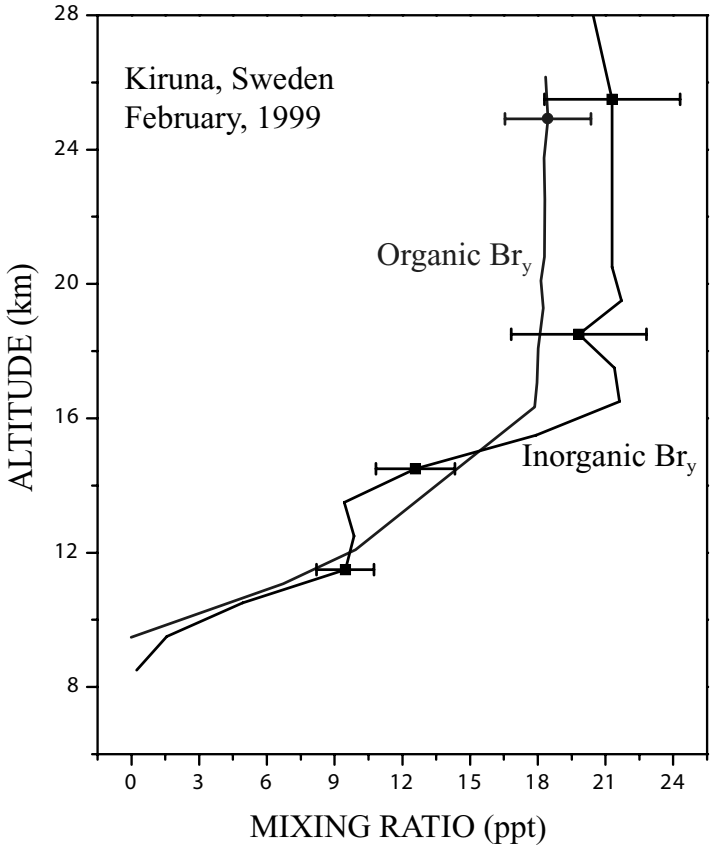

Figure 2.3-8. Vertical profile of total inorganic bromine based on the observed disappearance of brominated source gases ('Organic Br_y') and based on measured BrO and a model calculation of the BrO/Br_y ratio ('Inorganic Br_y'). Measurements were obtained in the Arctic vortex, above Kiruna, Sweden (67.9˚N), during the winter of 1998/99. From Pfeilsticker *et al.* (2000).

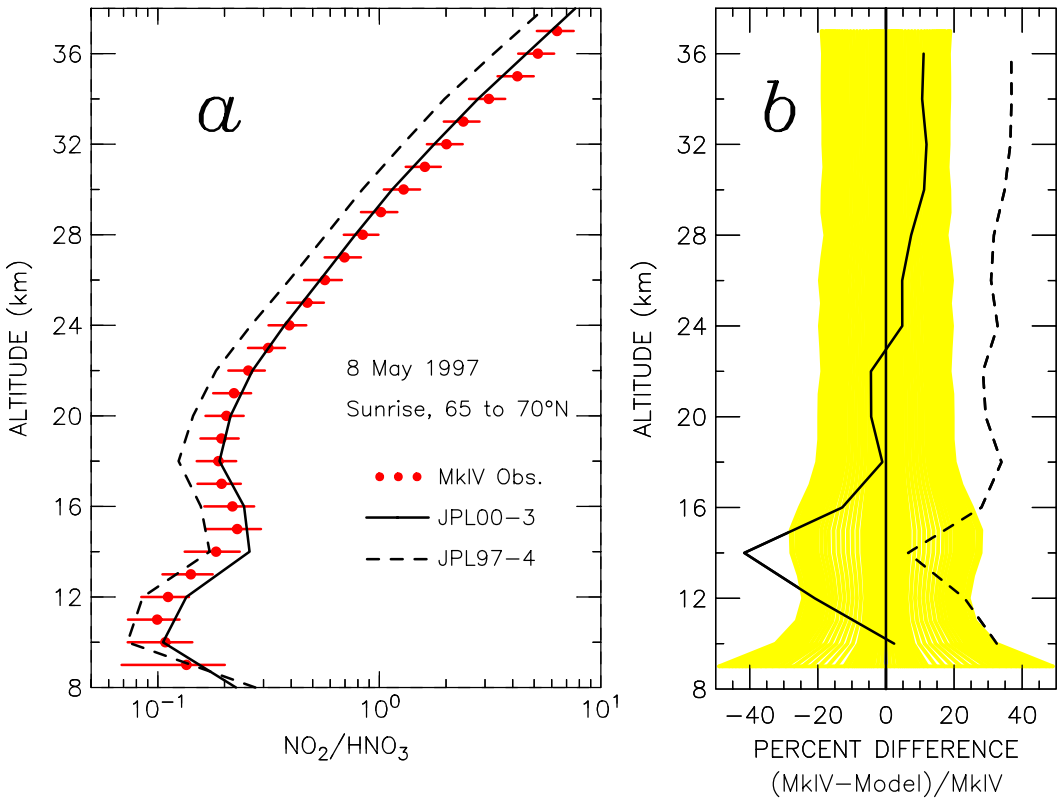

Figure 2.4-1. Panel *a*. MkIV observations (points with error bars) of the NO_2/HNO_3 ratio at sunrise obtained during a balloon flight in the Arctic stratosphere on 8 May 1997. Constrained photochemical steady state model calculations of the ratio, for the solar zenith angle of the observations, are shown for kinetic parameters from the JPL 00-3 evaluation (SOLID LINE) and from the JPL 97-4 evaluation (DASHED LINE). Error bars on the observations represent 1σ precision, based on considerations such as residuals in the spectral fitting, combined in quadrature with spectroscopic uncertainties. Panel *b*. Percentage difference between measured NO_2/HNO_3 and values from the two model calculations. The shaded region denotes the 1σ measurement uncertainty. After Osterman *et al.* (1999) and Salawitch et al. (2002b).

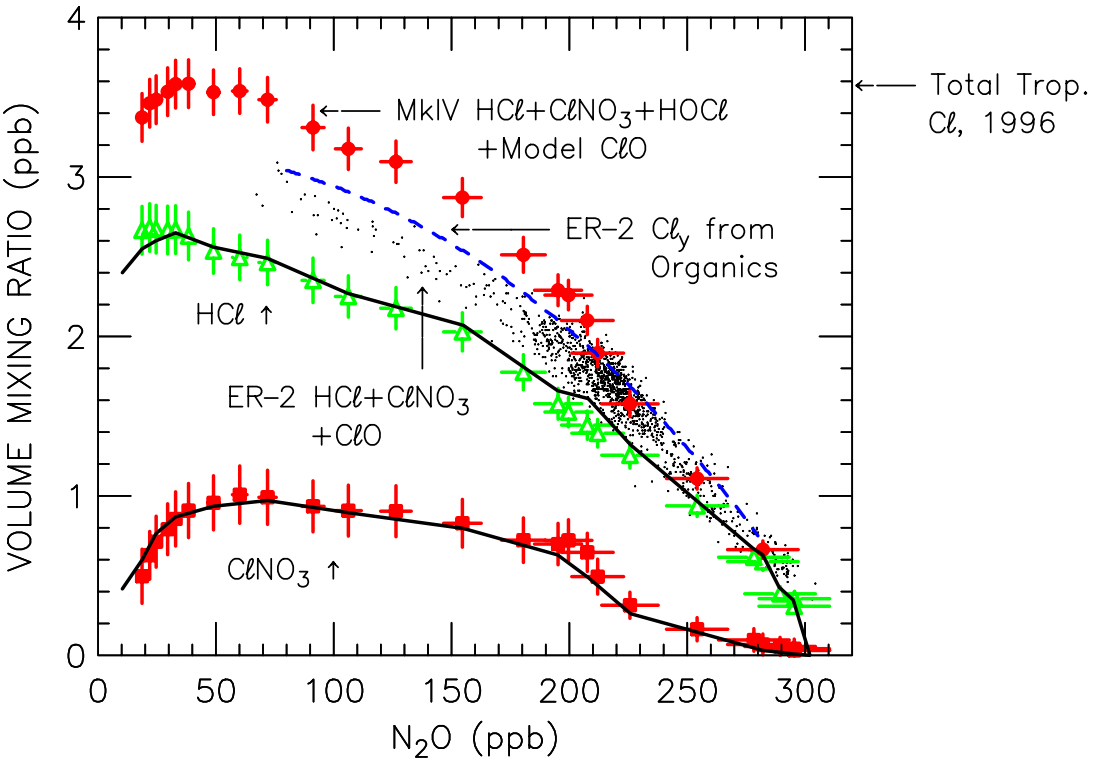

Figure 2.4-2. Measurements of chlorine species from balloon and *in situ* instruments during POLARIS. MkIV balloon-borne measurements of the volume mixing ratio of HCl (greeen triangles) and $ClNO_3$ (red squares) versus N_2O observed over Fairbanks, Alaska (64.8˚N) on 8 May 1997 are shown, along with calculated values of HCl and $ClNO_3$ (SOLID BLACK LINES) found using a constrained photochemical model (Sen *et al.* 1999, updated for JPL 00-3 kinetics). The DASHED BLUE LINE shows an estimate of Cl_y based on ER-2 measurements of the organic source molecules during POLARIS (Sen *et al.*, 1999). The sum HCl+$ClNO_3$+HOCl measured by MkIV plus calculated ClO (red circles) is also shown; calculated ClO makes a negligible contribution to this sum except for the highest altitudes (*e.g.,* $N_2O < 50$ ppb) because the MkIV observations are obtained at twilight. Error bars for the MkIV measurements represent 1σ precision. ER-2 measurements of the sum HCl + $ClNO_3$ + ClO are shown by the BLACK DOTS (Bonne *et al.*, 2000). Since the ER-2 observations are obtained at altitudes below ~20 km, species such as HOCl, Cl, etc. are estimated to make a negligible (*e.g.,* < 20 ppt) contribution to the sum and are therefore neglected. Finally, the arrow in the right margin denotes the total chlorine content, 3.59 ppb, of the entire suite of tropospheric organic compounds for 1996 (WMO, 1998, Table 1-2).

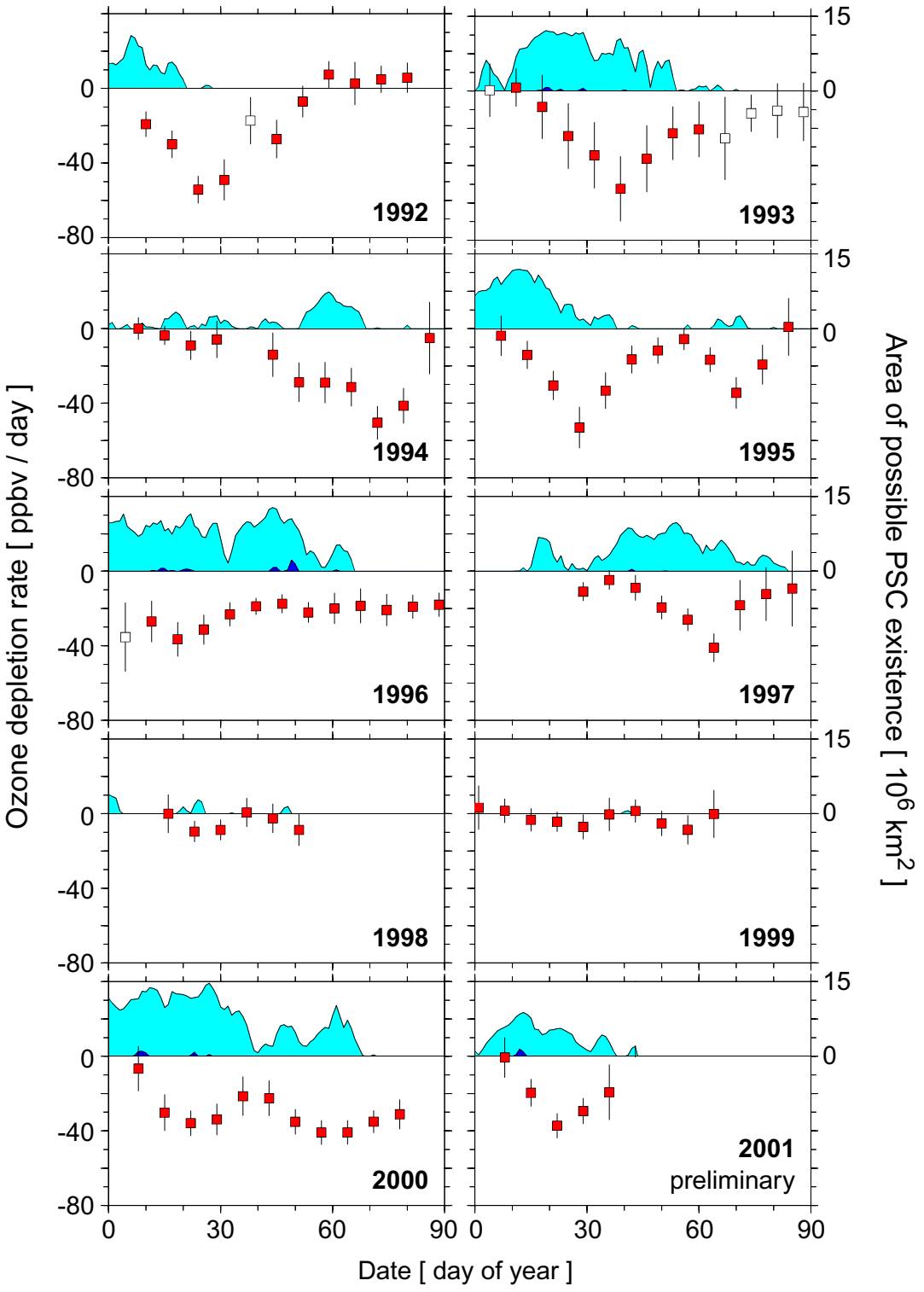

Figure 3-1. Ozone loss rates from Match at 475 K for various winters (squares) and A_{NAT} at 475 K (blue shaded areas).

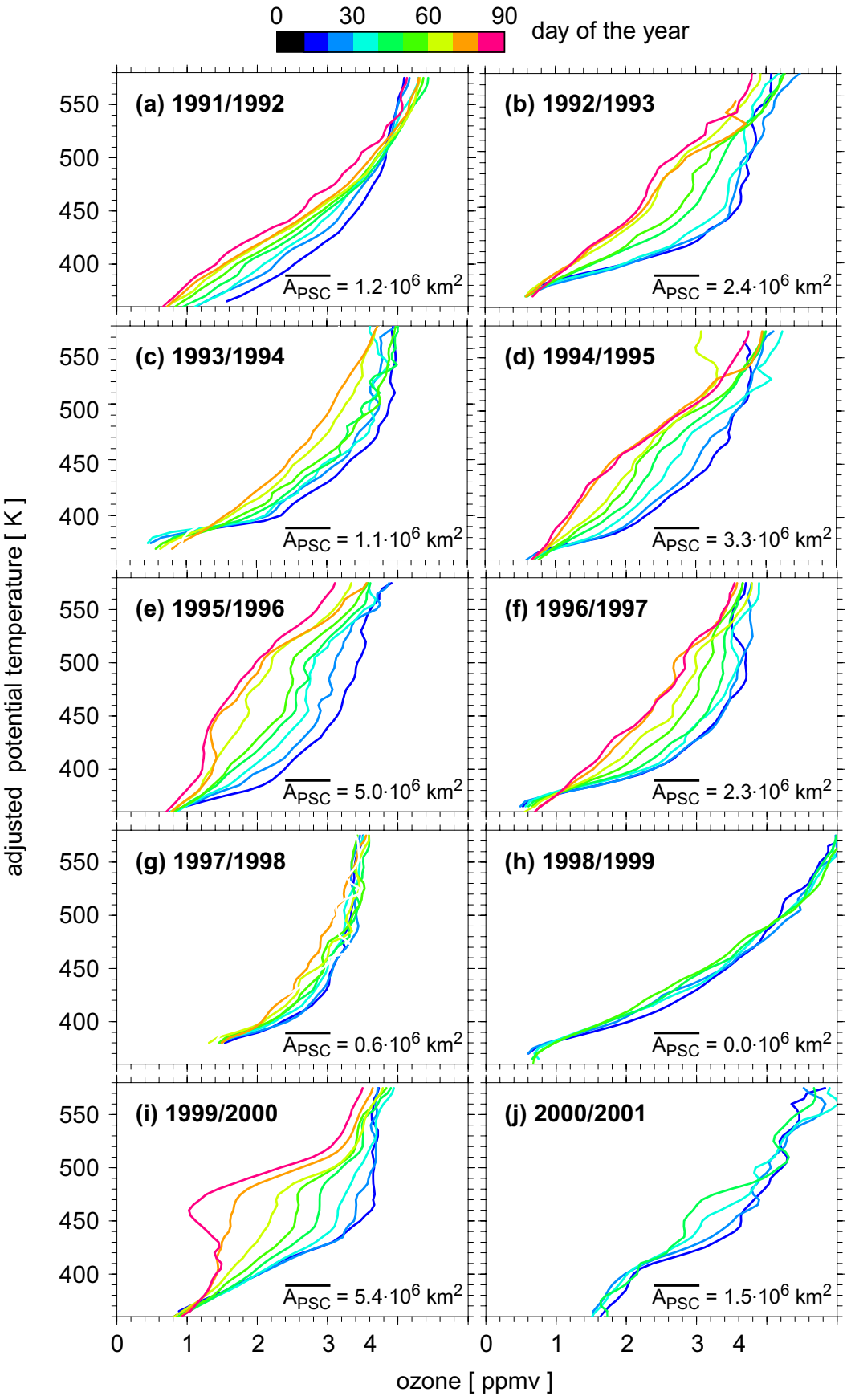

Figure 3-2. The evolution of the average ozone profile inside the polar vortex in spring-equivalent potential temperature (eΘ) coordinates for various years, see text for a definition of eΘ. The data from all ozonesonde measurements inside the vortex have been averaged into 10-day bins, centered around the day indicated by the color scale. The profiles typically rely on 20-50 individual measurements that in most cases sample the PV-space homogeneously. The black dotted lines show the average profile for 5 January (+/-5 days) with potential temperature as the vertical coordinate (i.e., subsidence not applied). The average values for A_{PSC} from 16 December to 31 March of each winter, between 400 and 550 K, are also given in each panel.

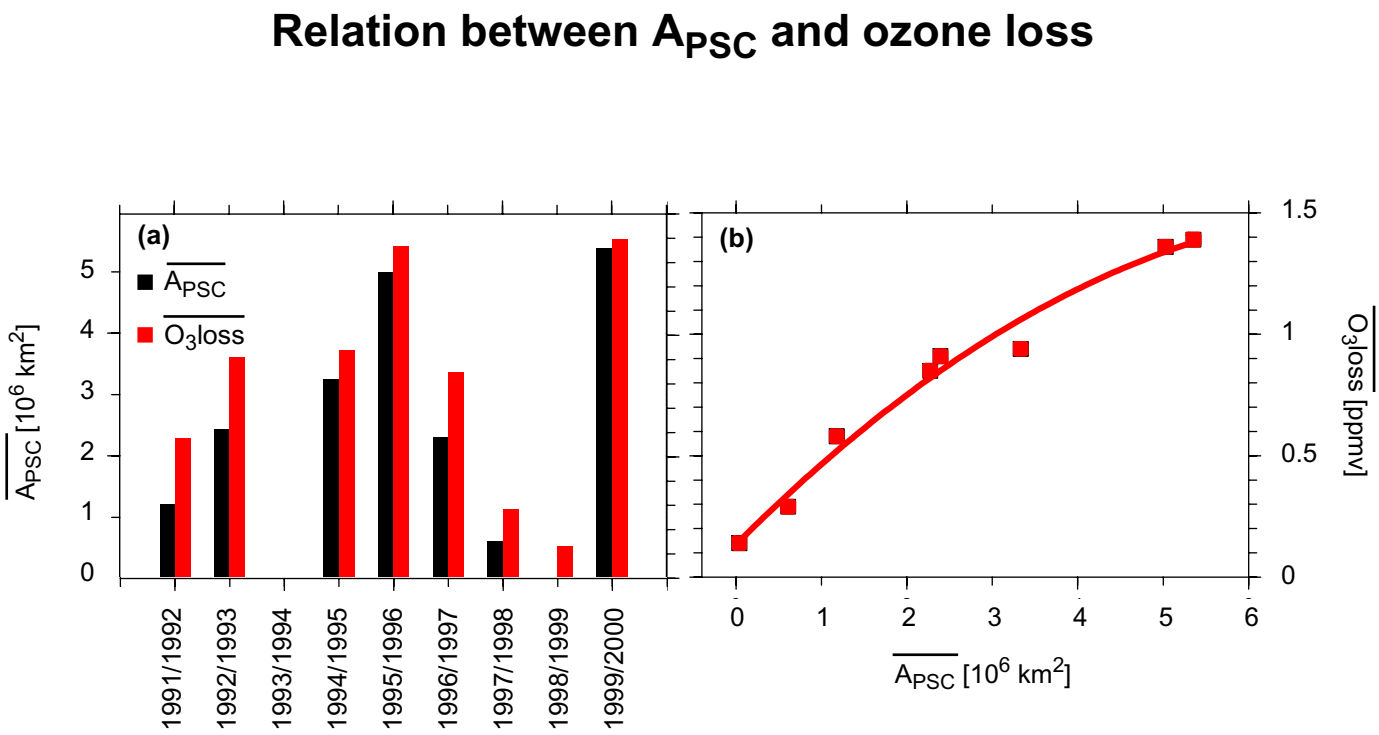

Figure 3-3. (a) Histogram of average values of A_{PSC} (black bars) and the average value for chemical loss of ozone from mid January to end of March, between 400 and 550 K (red bars). When the period of rapid ozone loss overlaps with the vortex break up, the vortex average approach can not be used to estimate the overall loss of ozone. These years (1994, 2001) have been omitted. (b) Scatter diagram of average ozone loss versus A_{PSC}.

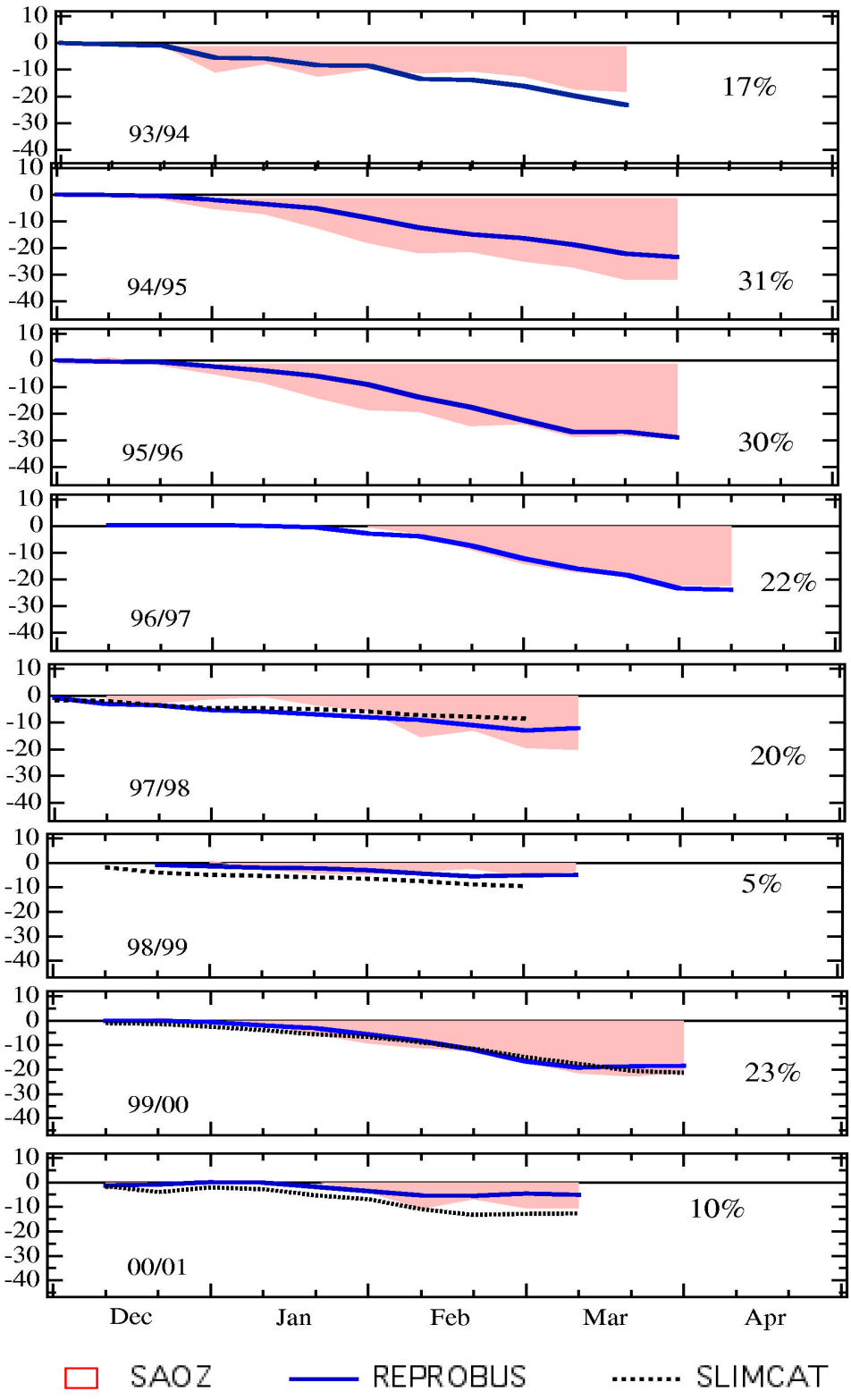

Figure 3-4. Total ozone reduction derived by comparing measurements of the SAOZ network with passive ozone in REPROBUS (pink hatched area) and modeled ozone losses (full line: REPROBUS, dotted line: SLIMCAT). F. Goutail

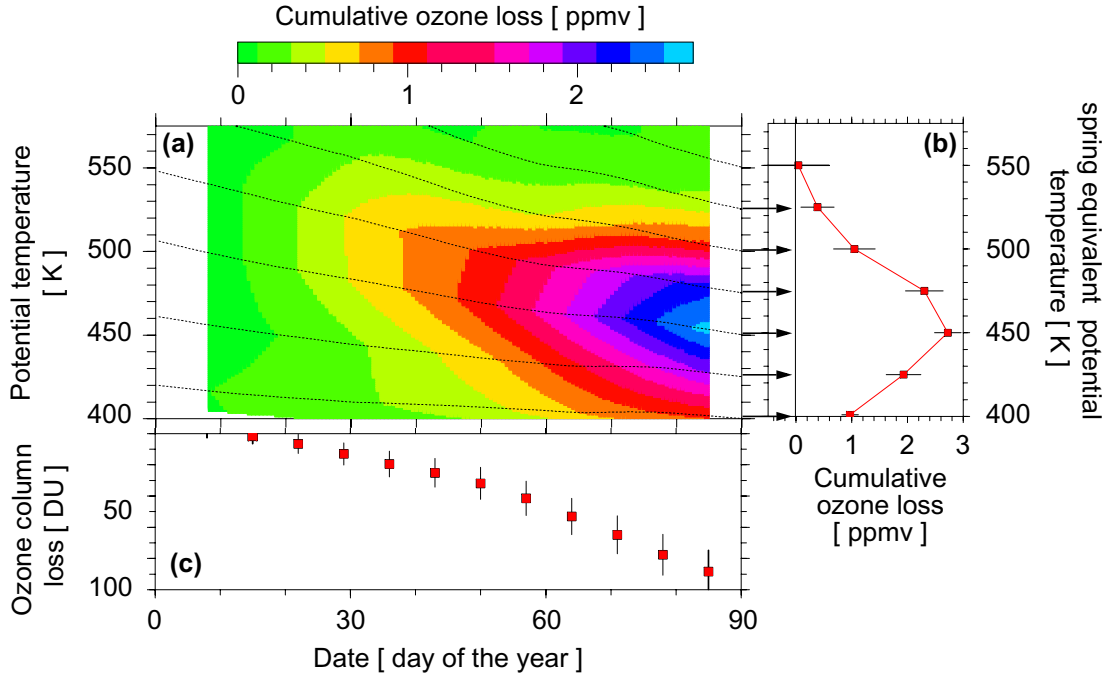

Figure 3-5. **(a)** Evolution of the accumulated ozone loss in subsiding air masses from Match. The subsidence of air is indicated by the black lines. The heavy black line is explained in the text. **(b)** Profile of the accumulated ozone loss on 26 March 2000 from Match. **(c)** Accumulated chemical ozone loss in the partial column between Q = 400 and 575 K from Match. Reproduced from Rex *et al.* 2001.

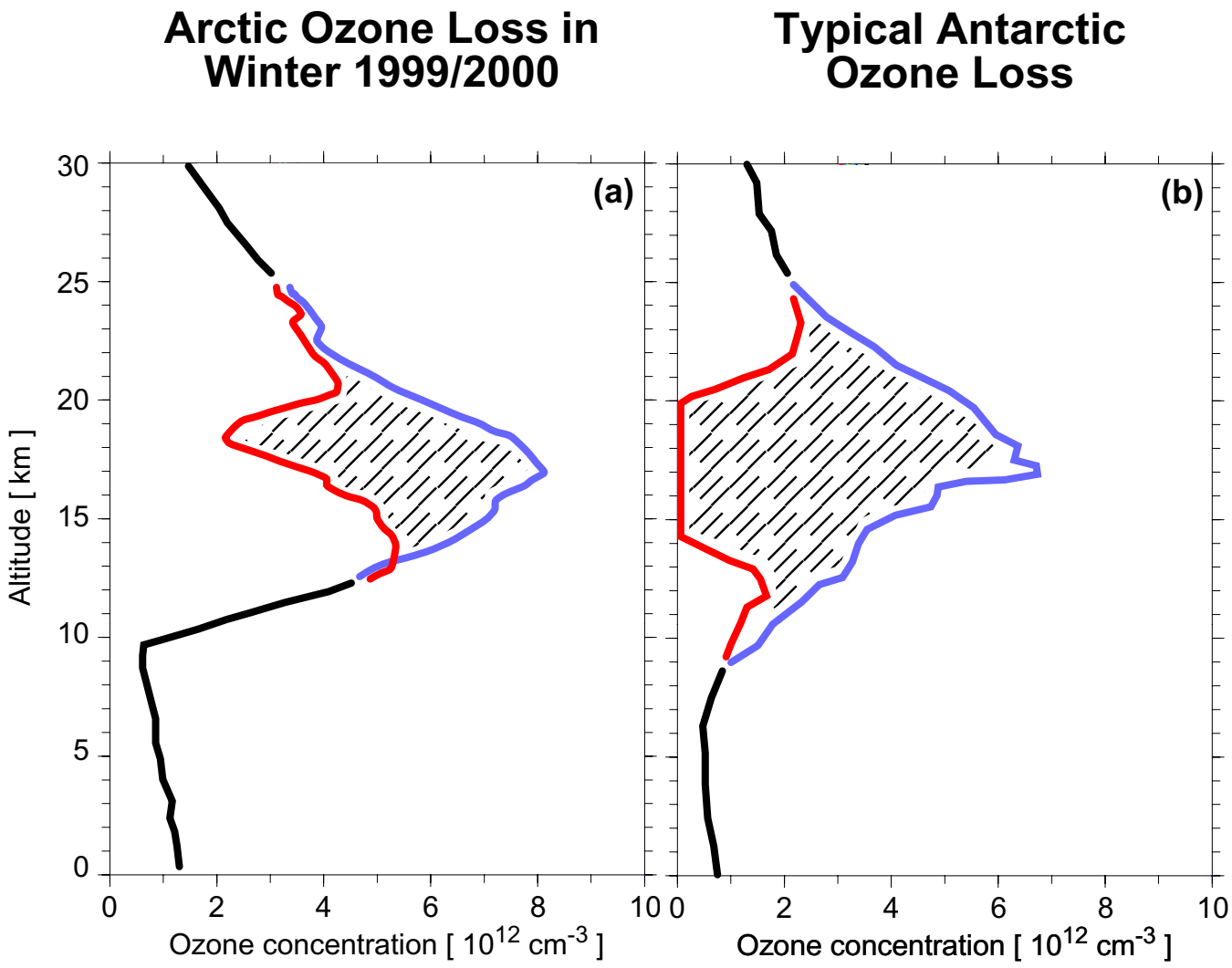

Figure 3-6. (a) Concentration profile of O_3 during late winter for observations from ozonesondes between 20 and 30 March 2000 (red). The profile of O_3* (blue), the abundance of O_3 expected in the absence of any chemical loss, is estimated by allowing the early winter vortex average O_3 profile from ozonesondes to descend by amounts based on cooling rates from the SLIMCAT model. For this calculation, the mixing ratio of O_3 is assumed to be conserved during descent and is converted to concentration in the last step. The profiles are shown for the altitude and pressure the air would have been at on March 25. The difference between the profile of O_3* and O_3 is hashed. This is an estimate, based on the vortex average approach, for the accumulated chemical loss of ozone during the winter. The black lines represent a typical late March ozone profile above and below the vertical region where significant ozone loss occurred. Adapted from Rex *et al.*, 2001. **(b)** Illustration of the typical degree of ozone loss in the Antarctic. Typical mid-winter (15 July 1997, blue) and late winter (13 October 1997, red) ozone profiles measured inside the Antarctic polar vortex at the Neumayer station at 71° S. This panel is for illustration only and no attempt has been made to correct for transport effects, which are weaker in the Antarctic compared to the Arctic.

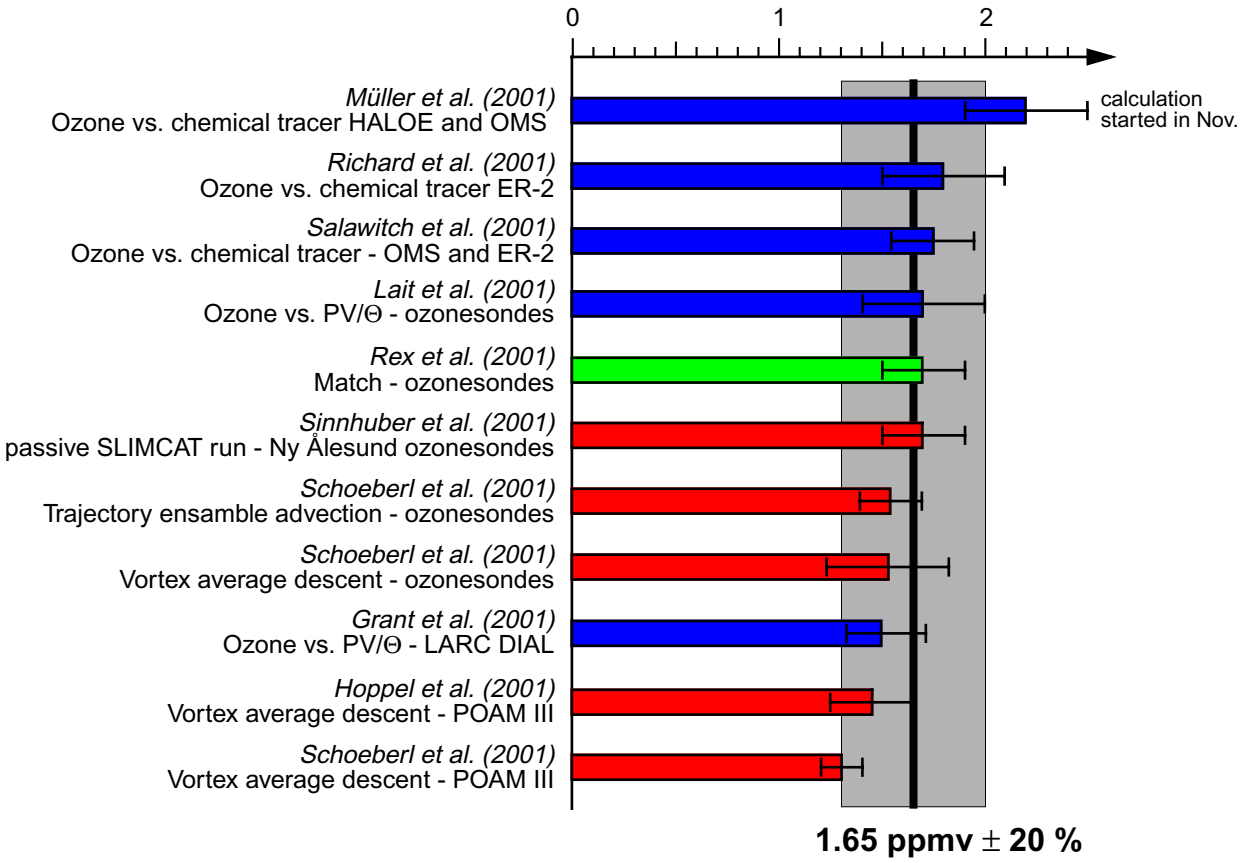

Figure 3-7. Overview over the results of various approaches to estimate the amount of ozone loss between January 20 and March 12. The results are stated for the layer of air that subsided from about 475 K at the beginning of the period to 450 K at the end. Results from studies that use the relation between ozone and an inert tracer are plotted in blue. Red color is used for studies that rely on bulk transport calculations. Results from the approach that relies on individual transport calculations is plotted in green. Based on Newman *et al.* (2001).

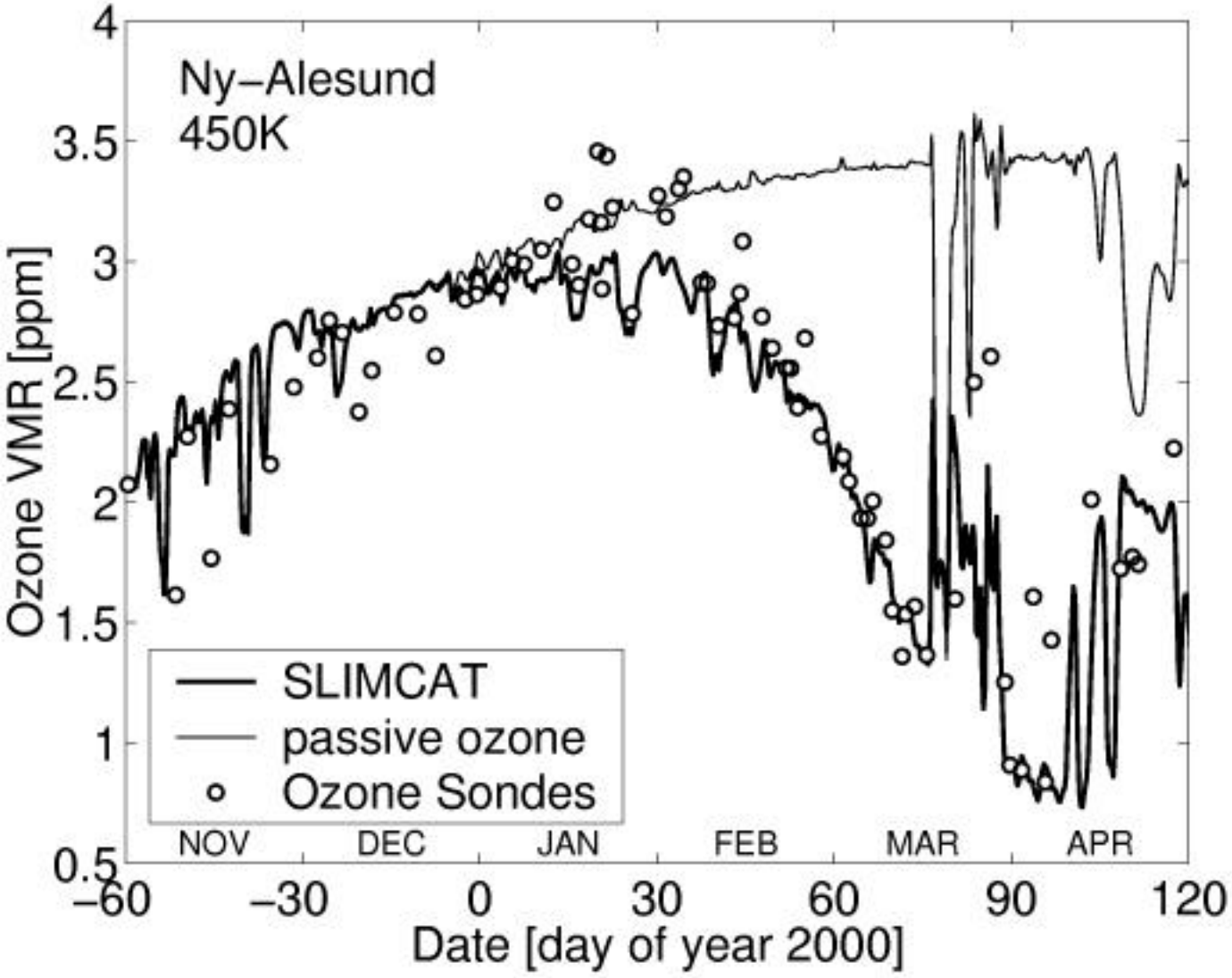

Figure 3-8. Ozone sonde measurements at Ny-Ålesund, 79˚N compared to the SLIMCAT three-dimensional transport model output for Ny-Ålesund at the 450 K isentropic level.

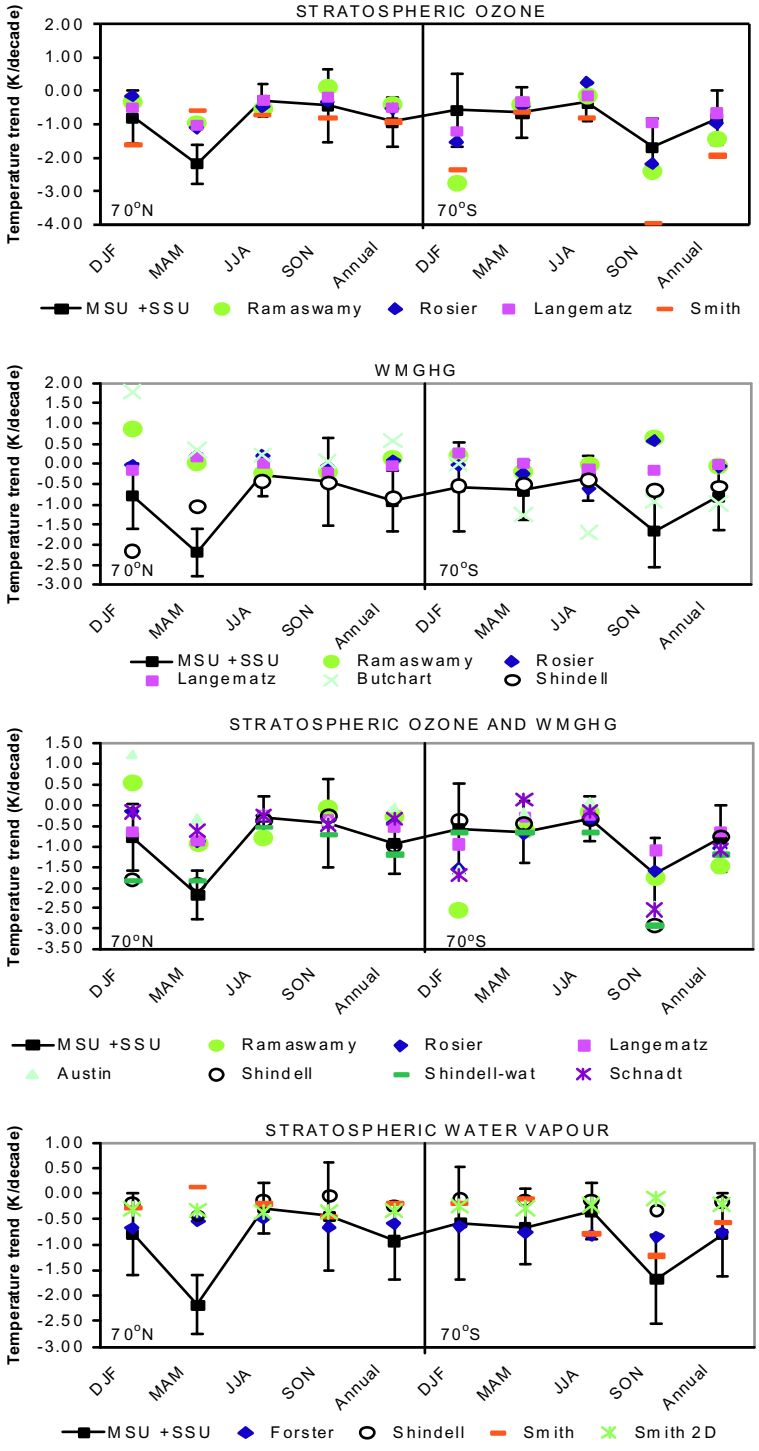

Figure 4.1. Shows the seasonal and annual combined 50 hPa and 100 hPa trend at 70˚N and 70˚S, corresponding to 1/3 of the 50 hPa trend added to 2/3 of the 100 hPa trend, using the data presented in Table 4.1. The modeled temperature trends are shown in four panels, for: a) stratospheric ozone changes; b) WMGHG changes; c) WMGHG and stratospheric ozone changes and d) stratospheric water vapor changes. On each panel 2-s error bars are plotted for the observed satellite trends.

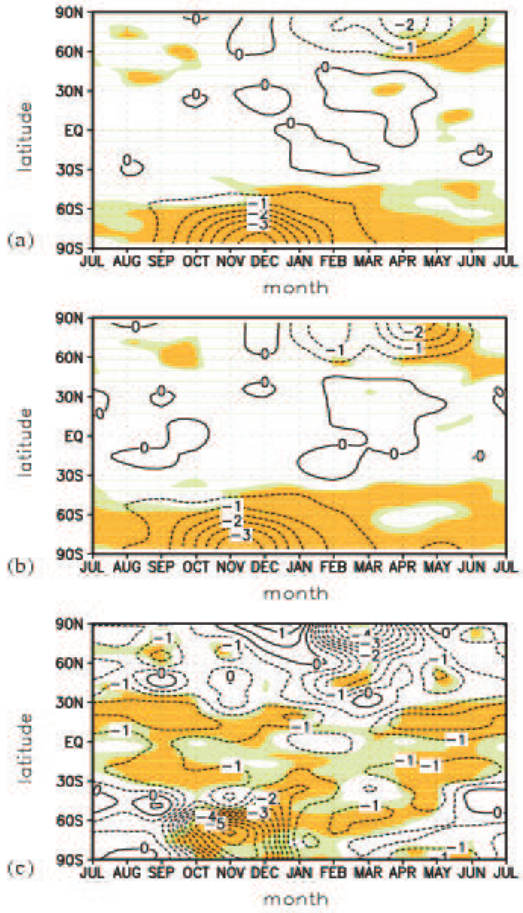

Figure 4.2. Annual cycle of the zonal-mean temperature trend (K/decade) at 100 hPa. Panels a) and b) show model derived trends: a) employing the observed 1980-2000 ozone trend and b) with an additional increase in CO_2. Panel c) shows the corresponding 1980-2000 linear trend, derived from NCEP–reanalysis data. The contour interval is 0.5 K/decade. Dark (light) shaded areas donate regions where the trend is significant at the 99% (95%) confidence level. (Figure from Langematz *et al.,* 2002).

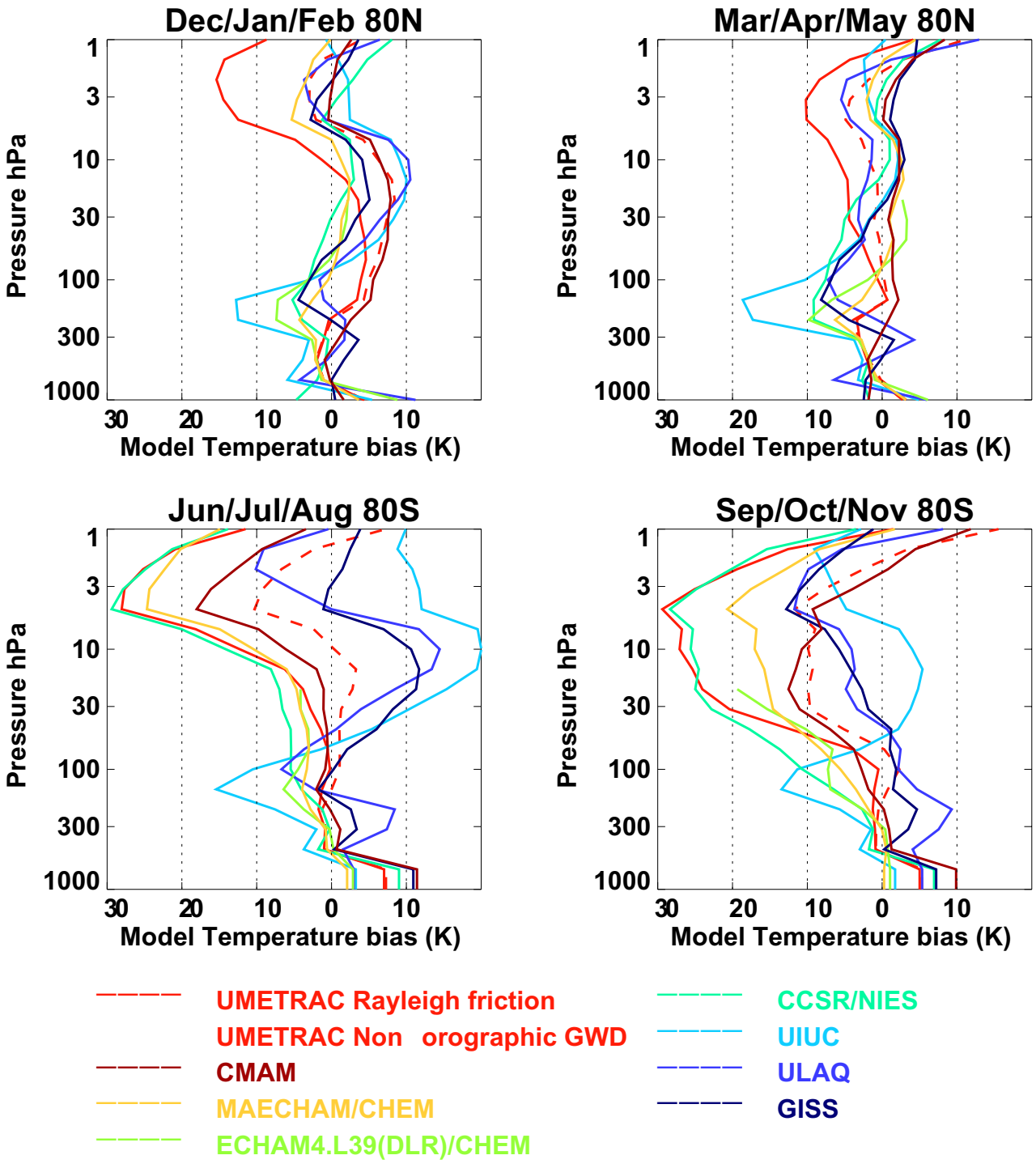

Figure 5.1. Temperature biases at 80˚N and 80˚S for the winter and spring seasons, as a function of pressure. To determine the bias, a climatology determined from 10 years of UKMO data assimilation temperatures was subtracted from the model results.

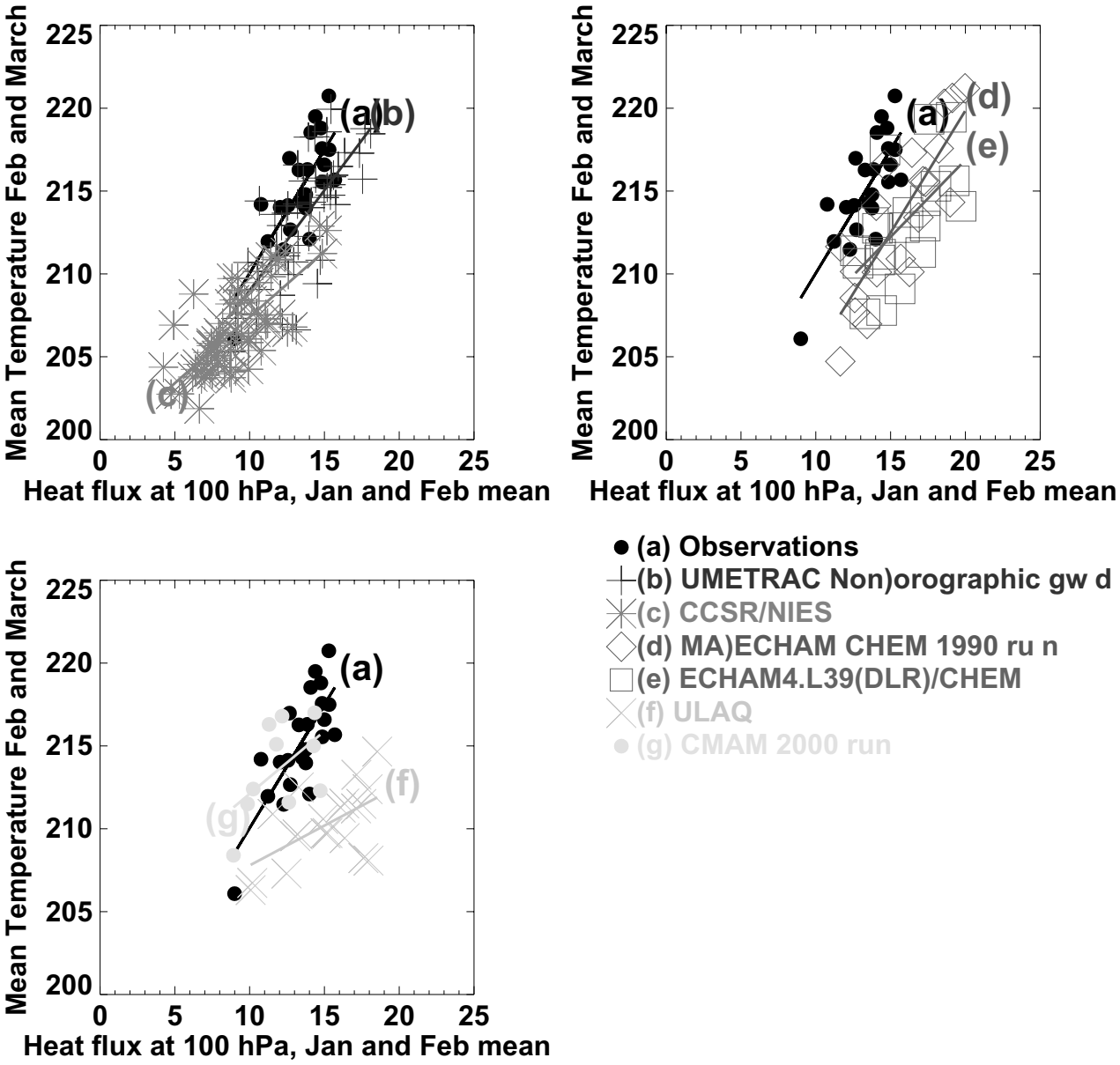

Figure 5.2. Scatter diagrams of the polar heat flux v'T' (averaged 40 to 80˚N, at 100 hPa for Jan and Feb) against temperature (averaged 60 to 90˚N, at 50 hPa for Feb and March) for participating models. The solid lines are linear regression lines between the two variables. The observations are taken from NCEP data. The heat flux is in units of Km/s, the temperature is in K.

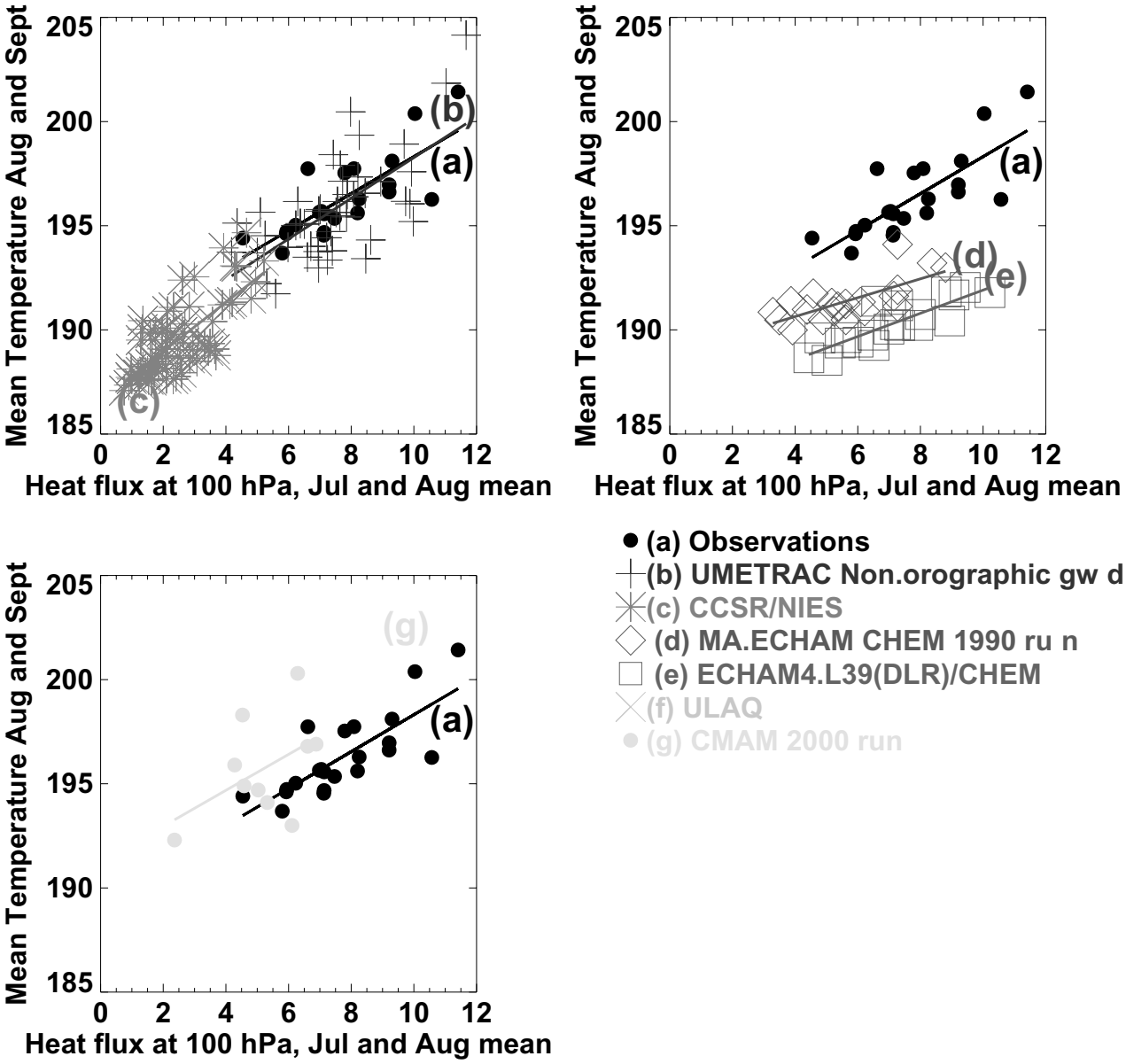

Figure 5.3. As in Figure 5.2, but for the Southern Hemisphere for the months July and August, and August and September respectively.

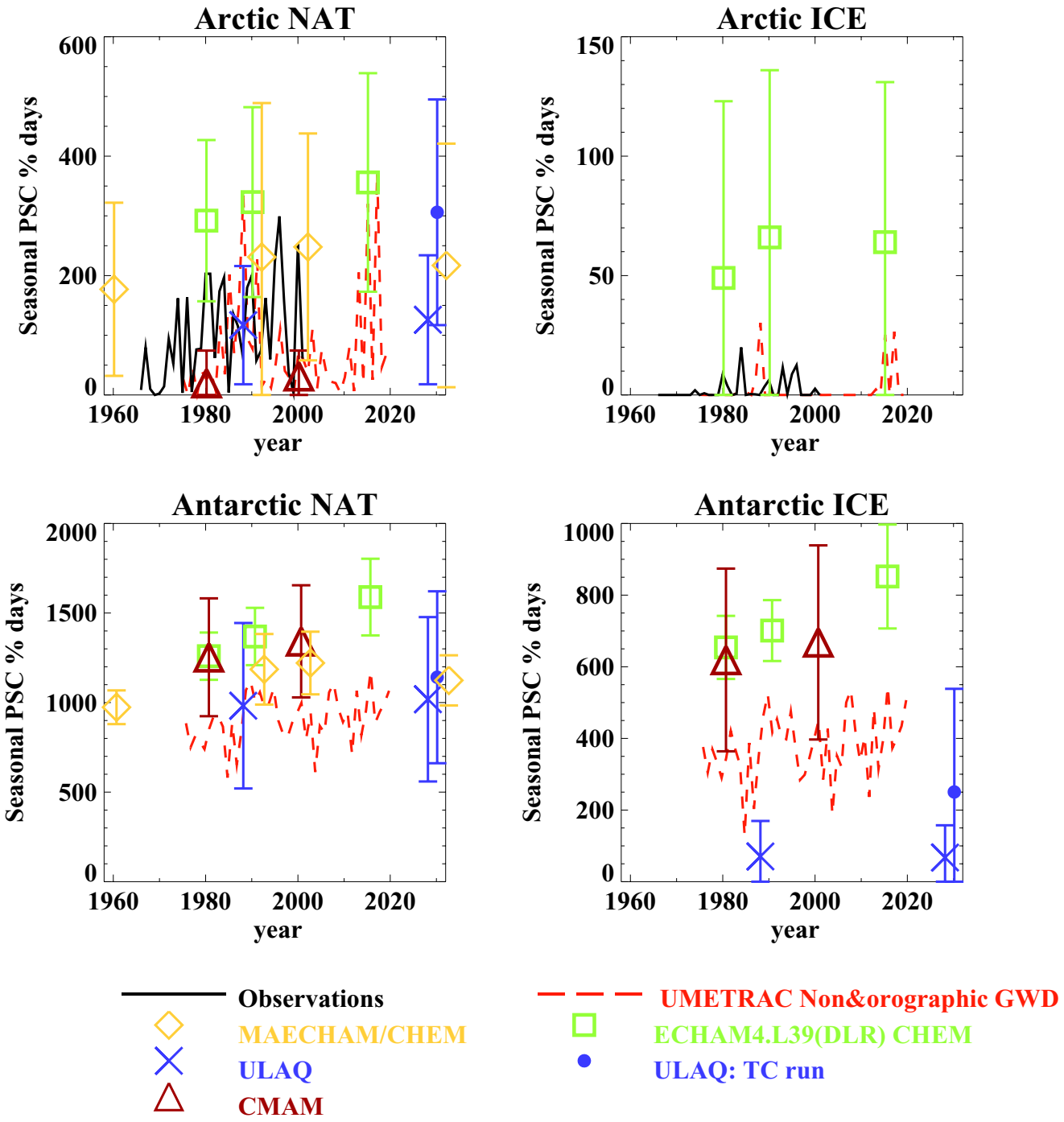

Figure 5.4. Seasonal integration of the hemispheric area at 50 hPa, corresponding to the temperatures below 195 K (approximate NAT temperature) and below 188 K (approximate ice temperature) for participating models. The error bars for the timeslice runs indicate 95% confidence intervals. For clarity, ULAQ data are plotted two years early, and for 1990 and 2030 MAECHEM CHEM data are plotted two years late.

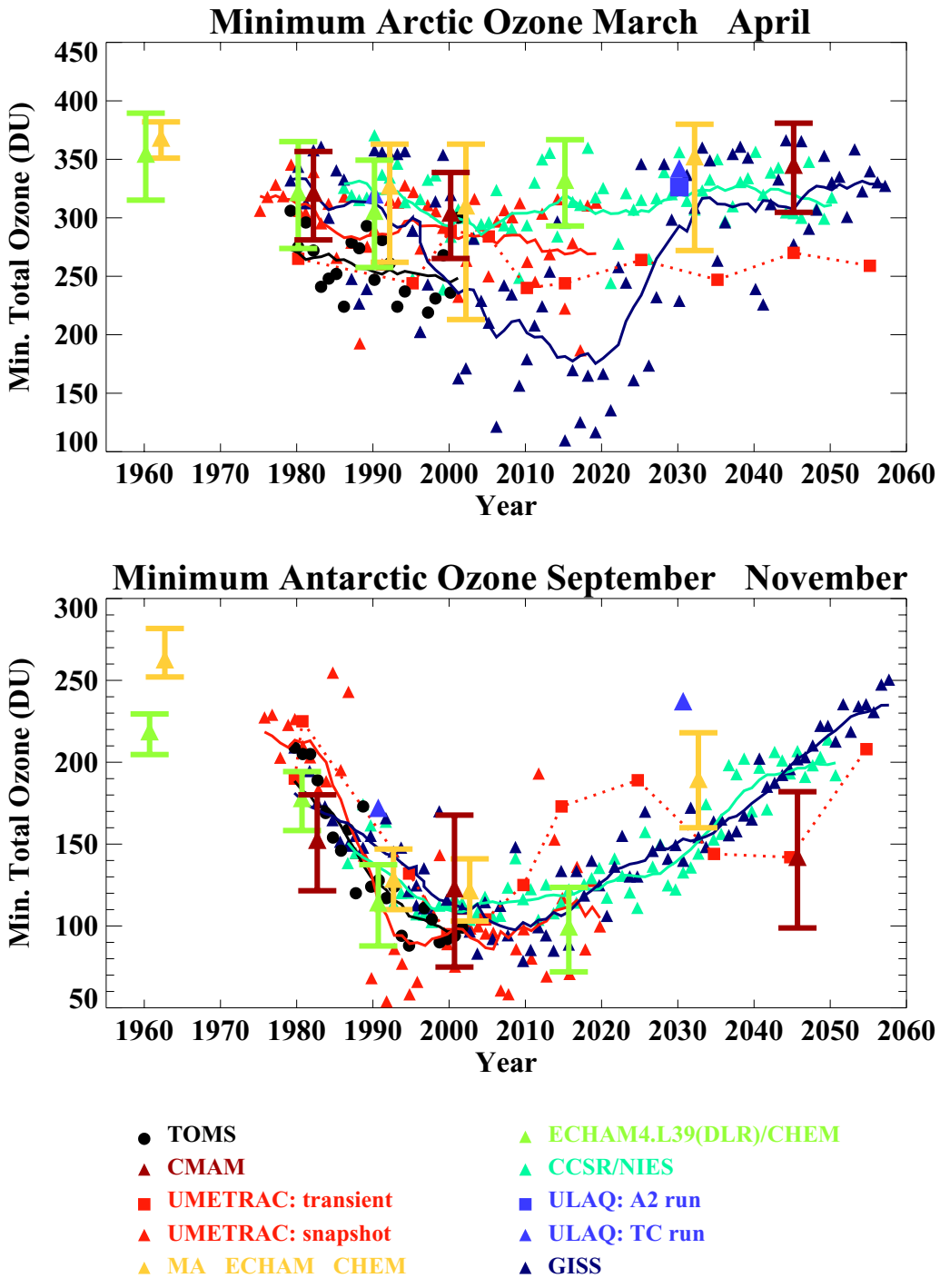

Figure 5.5. Minimum Arctic (Mar./Apr.) and Antarctic (Sep./Oct./Nov.) total ozone for participating models. TOMS data are used for comparison. The solid lines show running decadal averages for the transient model results and TOMS observations. The broken line shows UMETRAC snapshot model results. The results for ECHAM4.L39(DLR)/CHEM and CMAM indicate the mean and 2 standard deviations for 20-year and 10-year timeslice runs, respectively. The results for ULAQ are for one-year integrations of the model from equilibrium conditions. For the MAECHAM/CHEM results: (i) the mean and range of minimum values obtained in 20-year timeslice experiments for a model output frequency of once every ten days are plotted, which may have underestimated slightly the full range of values in the model, (ii) for clarity, the values are plotted two years late, (iii) to compute the columns, a standard tropospheric column of 40 DU (Southern Hemisphere) and 100 DU (Northern Hemisphere) have been added to the stratospheric columns.

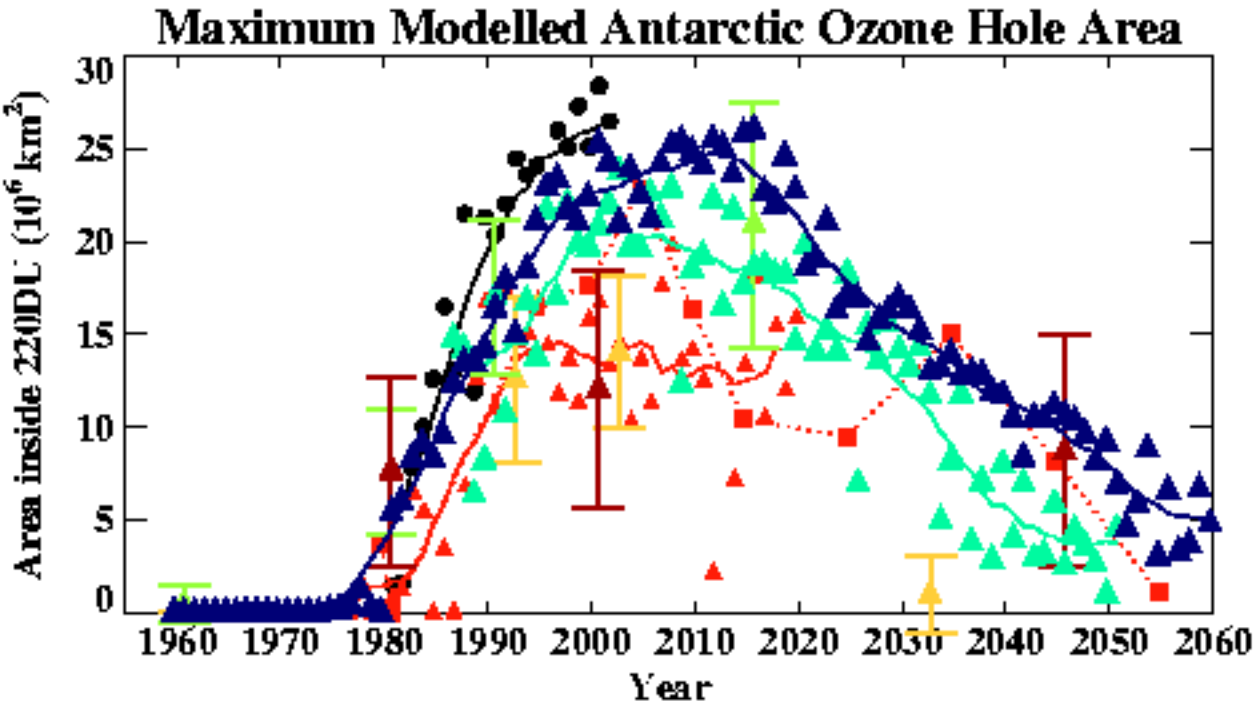

Figure 5-6. Maximum area of the Antarctic ozone hole, as given by the 220 DU contour for observations and participating models. See Figure 5.5 for line styles and symbols.